Characterizing the signature of a spatio-temporal wind wave field

AlviseBenetazzo[a] FilippoBergamasco[b] JeseonYoo[c] LuigiCavaleri[a] Sun-SinKim[c] LucianaBertotti[a] FrancescoBarbariol[a] Jae-SeolShim[c]

https://doi.org/10.1016/j.ocemod.2018.06.007

Abstract

This study aims at characterizing the distinctive features of a spatio-temporal nonlinear wave surface. We analyze wind-generated 3-D wave fields observed during the passage of an atmospheric front, which led to a wide directional spreading of wave energy. Data were acquired from the ocean research station *Socheongcho-ORS* (Yellow Sea) with a stereo wave imaging system. They include 3-D (i.e. 2-D + time) measurements of the sea surface elevation with high spatial and temporal resolution over a swath larger than any previous similar deployment. We examine the shape and the nonlinear properties of the wavenumber/frequency 3-D wave spectrum, and the characteristic spatial, temporal and spatio-temporal length scales of the wave field. We then focus on analyzing the probability of occurrence and the spatio-temporal size of the rogue waves we identified in the data. In particular, we provide for the first time an empirical estimate of the extent of the horizontal sea surface spanned by rogue waves. We also propose and assess a novel strategy to determine from the 3-D wave spectrum the vertical current profile, to be then used to map the spectrum on intrinsic frequencies.

Keywords

Wind waves
Spatio-temporal length scales
Stereo wave imaging
3-D wave spectrum
Extreme waves
Rogue waves

1. Introduction

The wind-generated waves we observe in the open ocean have shape and direction that vary irregularly with time and space. The basic model for describing the moving surface elevation field is the random-phase amplitude model (Pierson et al., 1955), then used to represent the wave field as a Gaussian process, i.e. as the sum of a large number of harmonic wave components with different amplitude, period (hence wavenumber), direction, and phase. However, most of the time the sea state is represented using the frequency-dependent variance density spectrum (typically computed from time series of sea surface elevations), neglecting the dependence on direction and assuming as known the frequency–wavenumber relationship. Even so, in the years, attention has been paid also to the analysis of the 2-D sea surface spatial topography, starting from the seminal work of Cox and Munk (1954), up to recent observations using airborne scanning lidar systems (e.g. Hwang et al., 2000a, Romero and Melville, 2010) which allow representing the wave spectrum as a function of the wavenumber vector. A spatial statistics has been developed accordingly to analyze the relation between the 2-Dimensional energy spectrum of a Gaussian wavy surface and its observable statistical properties (Longuet-Higgins, 1957). In mathematics this analysis has been extended to manifolds to investigate the geometry of *N*-Dimensional random fields (Adler and Taylor, 2007, Piterbarg, 1996). In particular, for the analysis of the extreme values of linear and nonlinear wave fields it is mandatory to take full account of the spatial dimension (Baxevani and Rychlik, 2004, Boccotti, 2000, Fedele et al., 2012, Forristall, 2000, Krogstad et al., 2004, Lindgren, 1970).

In the ocean spatial and temporal length scales are not decoupled. This is the typical case of the dispersion relation whose assessment requires the 3-D wavenumber/frequency spectrum to be computed only using spatio-temporal (ST) wave data. Their field of application is wide and includes (but it is not limited to) the analysis of the bi-modality of the directional spectrum (e.g. Peureux et al., 2018), the detection of rogue waves (Benetazzo et al., 2015), the estimate of the sea currents (e.g. Senet et al., 2001), the observation of breaking ocean waves (Schwendeman and Thomson, 2017), the analysis of the linear and nonlinear spectrum (Leckler et al., 2015), the study of wave-ice interaction (Campbell et al., 2014), the analysis of wave-wave interactions (Aubourg et al., 2017). In general, considerable differences are found in sets of wavenumber spectra derived from

direct spatial measurements and from conversion of the frequency spectrum calculated from temporal measurements (Plant, 2009). This has serious implications, for instance, in the estimation of the sea surface roughness (Hwang, 2006).

From a technological point of view, there is a number of systems that allow the observation of time and space separately, in so providing reliable ST wave fields. The most widely used instruments are the stereo wave imaging (e.g. Benetazzo et al., 2012, Gallego et al., 2011) and the X-band marine radar (Nieto Borge et al., 2004, Young et al., 1985). As a general rule, the latter allows covering a large swath (up to $\sim 5 \times 5$ km^2), but it requires strong assumptions to invert the radar signal. On the contrary the former is an accurate and direct measurement system, but it has constraints on the maximum area ($\sim 10^3$–10^4 m^2) that can be observed. In this study, to empirically characterize the distinctive features of a spatio-temporal, random, moving nonlinear wave surface, we take advantage of a spatio-temporal wave record collected using a stereo wave imaging system, based on the Wave Acquisition Stereo System (WASS; Benetazzo et al., 2015, Benetazzo et al., 2012). The WASS cameras were installed on the ocean research station *Socheongcho-ORS* (Yellow Sea, Fig. 1) in a configuration allowing a relatively large sea surface region to be framed. We focus specifically on the characterization of the 3-D spectrum and typical length scales of the ST wave field. We follow an approach similar to the one used by Zavadsky et al. (2017) for the description of the two-dimensional structure of short gravity waves in a wind wave tank, but we extend the analysis to three-dimensional fields (hence including time) and focus particularly on the characterization of the highest (eventually rogue) waves of the ST record.

Fig. 1. (left panel) Geographical map of the Yellow Sea and the three Korean ocean research stations (ORSs). *Socheongcho-ORS* is the northernmost tower. (right panel)

Southerly view of the *Socheongcho-ORS*. Stereo cameras were installed on the east side at the penultimate floor (33 m high), underneath the protruding roof.

The short- and mid-term goal of the installation is to accurately characterize the nonlinear properties of a ST sea surface elevation field measured using a directional phase resolving instrument, with the specific purpose of determining the size and likelihood of rogue waves. In particular we want to assess how common these waves are in any sea condition. In the longer-term, the aim is to deploy the WASS technology on all the three towers of the *ORS* system (Fig. 1), in so doing improving the knowledge on the possible wave conditions in the Yellow Sea and on the likelihood of extreme waves during severe wind conditions, including typhoons.

The paper proceeds as follows. Section 2 describes the stereo system and the metocean conditions during the wave data acquisition. In Section 3, we characterize the distinctive scales of the wave field. In Section 4, we use the spatio-temporal features of the sea state to analyze the likelihood and size of rogue waves. A novel method to estimate the vertical current profile from ST wave data is presented in Section 5. Section 6 provides the conclusions of our study.

2. Data overview

In this section, we describe the wave data acquired in the Yellow Sea from the ocean research station *Socheongcho-ORS* (Fig. 1; latitude = 37°25′23.28″ N and longitude = 124°44′16.94″ E; the local depth d is on average 50 m) managed by the Korea Institute of Ocean Science and Technology (KIOST). For the analysis of the ST sea surface elevation directional field, we selected a stereo-image sequence recorded on 13 May 2017, when a dynamical meteorological cold front passed at the station position, leading to a rapid evolution of the local wave conditions, and eventually mixed sea conditions.

2.1. Metocean climate of the eastern Yellow Sea

The sea west of Korea can be classified as a tide-dominated environment in the eastern flat shelf of the Yellow sea basin. Coastal currents and circulations are mainly forced by large tides with range of several meters. The tidal excursion in the central part of the west coast is typically between 3 m and 6 m with a semi-diurnal inequality. The tidal currents are up to more than 1 m/s (see Section 5).

Winds and waves in this area show the characteristics of a monsoonal climate. In winter, large wave events (i.e. with significant wave height > 2 m) tend to occur frequently along the west coast due to the northwesters caused by low-pressure systems on East Asia. In summer, except for occasional typhoons, tropical high atmospheric pressures from the Northwest Pacific Ocean generally suppress winds and make waves mild or moderate over the Yellow Sea. The yearly mean significant wave height (wave-gauge station) near the Socheong island is reported to be about 1 m (KORDI Korean Ocean Research and Development Institute, 2003). Largest significant wave height observed in recent years in the central west waters range from 4.0 m to 6.5 m, with periods of 7.5–11.0 s (Oh et al., 2015).

The summer typhoons are typically generated in the Northwest Pacific Ocean and move northward towards the Korean peninsula. Around Korea typhoons occur from July till October, most frequently in September. They impact on the central west waters is more limited than on the more southern coastal seas of Korea, since in general they tend to move in the north-east direction passing south of Korea. However, when a typhoon passes through the Yellow Sea, it may bring severe impacts along its west coasts. For instance, the most devastating typhoon (i.e. named *Bolaven* in 2012) recorded over the past decade caused significant wave height of 5.7 m in the central west waters (unpublished internal data at KIOST).

2.2. Stereo wave imaging

Since the profile of wind-generated waves observed in the open ocean changes rapidly and irregularly with time and space, full spectral and statistical properties of waves (including extremes) can be obtained only relying on 2-D sea surface elevation fields $z(x, y)$ function of time t and the horizontal sample space x=(x,y), i.e. $z = z(x, y, t)$. For our purpose, we analyze a spatio-temporal wave record $z(x, y, t)$ starting at 05 UTC on 13 May 2017, that we collected using a WASS. To this end, a couple of visible-range, synchronized digital cameras (8-bit grayscale, with 2456 × 2048 pixel resolution and 3.45-μm square active elements) mounting 8-mm distortionless lenses, were placed 5.04 m apart and 33 m above the mean sea level on the east side of the station (Fig. 2). The cameras were rotated down-looking with an inclination angle of about 25°. Image pairs were collected for a time interval D of duration $D = 600$ s, with a frame rate of 10 Hz.

Fig. 2. The WASS installed on the *Socheongcho-ORS*. The two cases holding the digital cameras are seen in the horizontal position used for alignment, before being inclined down-looking in their operative position.

The stereo-image processing relies on the same pipeline used in previous WASS deployments. It is based on a modified version (Bergamasco et al., 2017; code freely available at http://www.dais.unive.it/wass/; see also https://github.com/fbergama/wass) of the dense-stereo matching algorithm designed by Hirschmüller (2008), released within the Open Source Computer Vision library (Bradski and Kaehler, 2008; http://opencv.org), in order to match with sub-pixel resolution all common pixels of each stereo-image pair. The semi-global nature of the algorithm has the great advantage that it can relate the photometric consistency of several matching pixels to improve the reliability of the disparity map, especially for areas with loosely distinctive features. Given the wide field of view available from the height of 33 m, we made a sensitivity test for the stereo processing parameters, the main one being the matching-window size. We found that the size of 13 × 13 pixels set up as default in the WASS pipeline still allowed a precise localization of the correspondences between images, and it was thus adopted in our analysis. Other parameters of the stereo WASS pipeline (including the calibration of the pose between the cameras) were left to default

values (Bergamasco et al., 2017). For each image pair, the dense-stereo algorithm execution found on average 3.6 million corresponding points, which were reduced of about 1% with the optimization and cleaning of the disparity map, including the graph-based filtering process. Along the whole sequence of 6000 image pairs, about 21.6×10^9 triplets of (x, y, z) points resulted from the stereo process. Following the standard procedure, after the stereo processing, the 3-D wave field (x, y, z) at each time t was horizontally aligned with the xy-plane fixed on the mean sea water level (Benetazzo, 2006, Gallego et al., 2008). In this configuration, on the station, the y-axis coincides with the zonal direction (east–west), while the x-axis coincides with the meridional direction (north–south). Finally, 3-D scatter points were bi-linearly interpolated on a horizontal xy-grid with uniform spacing of 1.0 m. A few local inhomogeneous light reflections were visible in the far field that would hinder the accuracy of the stereo processing. To reduce their influence (see Appendix A), we have limited the region observed by the stereo system to 210 m from the platform along the y-axis (Fig. 3). Even so, the 2-D sea surface region Γ observed with WASS has an area $A \approx 21500$ m^2, at least 7 times larger than the region covered by any previous deployment of a stereo wave imaging system on a fixed platform (2900 m^2 in Benetazzo et al. (2015), 300 m^2 in Leckler et al. (2015), 4 m^2 in Banner et al. (1989), 12 m^2 in Kosnik and Dulov (2011), 2000 m^2 in de Vries et al. (2011)). It is also comparable with the area retrieved by the pioneering airborne system used by Holthuijsen (1983).

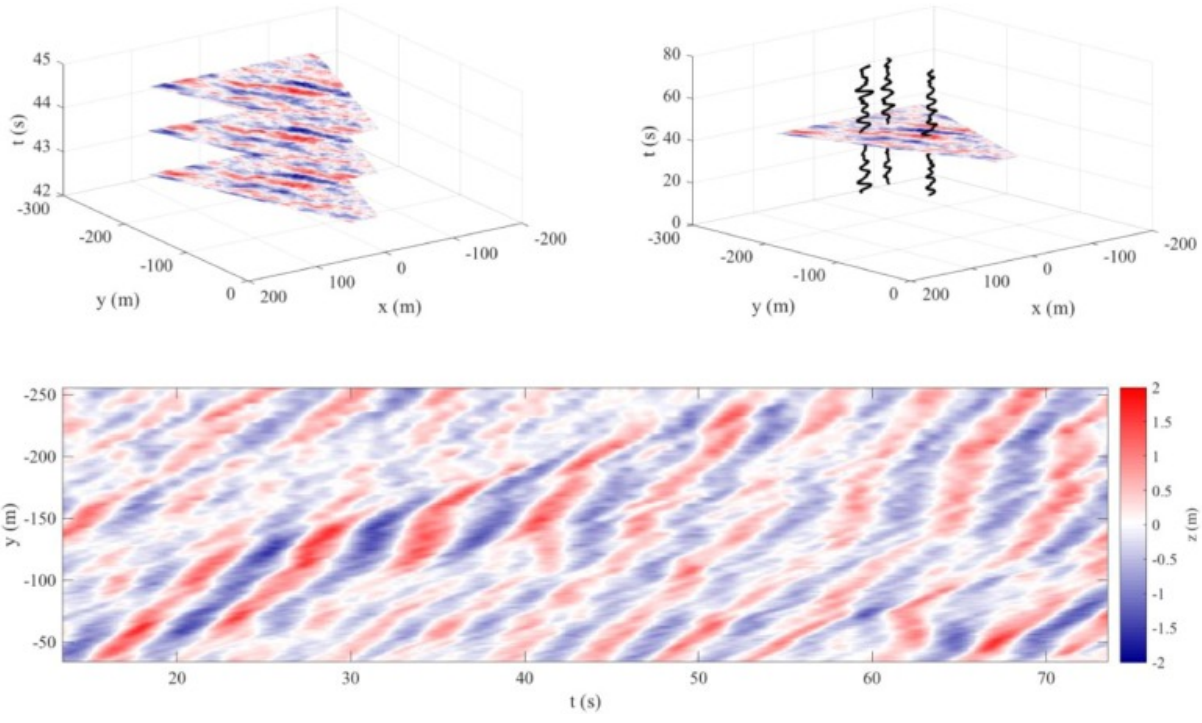

Fig. 3. Schematic representation of the ST sea surface elevation field $z(x, y, t)$ measured with WASS. (top-left panel) Sections on the horizontal xy-plane at different instants (the colorscale is proportional to the value of z). (top-right panel) Time series $z(t)$ at different locations on the xy-plane. (bottom panel) Hovmoller yt-diagram along the transect $x = 0$ m.

2.3. Wind and wave conditions

To analyze the metocean conditions in the Yellow Sea on 13 May 2017, we have used wind and wave forecasts of the Integrated Forecasting System (IFS) of the European Center for Medium-Range Weather Forecasts (ECMWF). The use of the +25–36 h twice a day forecast fields has been dictated by the possibility of having fields at 1-hour interval, which was required to follow the cold front. The Tco1279 meteorological model (see https://www.ecmwf.int) of the IFS system provides wind fields at 9-km resolution. The phase-averaged WAM wave model (Komen et al., 1994) is two-way fully coupled to the meteorological model. Janssen (2008) provides a full description of the so-called ECWAM version of the model as adapted to the local system. It is run on a spherical Gaussian grid with 14 km resolution using 36 frequencies ($f_1 = 0.0345$ Hz with 1.1 geometric progression) and 36 equally spaced directions (from 5° to 355° N). Model data have been downloaded on a regular grid with 0.1° resolution. The area spans from 30° N to 41° N and from 117° E to 130° E.

Fig. 4 provides the 10-m height wind maps at 00 and 04 UTC on 13 May. At 00 UTC, we can observe an extended wind conditions affecting the *Socheongcho-ORS* from southwest. This can be considered as a pre-frontal wind condition. Indeed around 04 UTC a meteorological cold front moving southeast crossed the station position, leading to a rapid turning of the wind direction, now from northwest. Indeed, after the passage of the front, at 05 UTC, the local incoming direction of the wind at the *Socheongcho-ORS* changed to about 300° N (Fig. 5). Model data were complemented with in-situ wind measurements (Fig. 6) from a Wind Monitor MA (RM Young) installed 50 m above the mean sea level, and wave measurements from a MIROS RangeFinder™. Consistently with the model data, on early 13 May, observations show a south-westerly wind blowing above 10 m/s, that rapidly intensified after 02 UTC when at the station it exceeded 14 m/s, peaking at 16 m/s at the time of the WASS acquisition (dashed red lines in Fig. 6). We note that in the hours before the data recording, the observed wind

incoming direction moved of 115°, from 180° N (at 00 UTC) to 295° N at 05 UTC, when MIROS recorded a sea state with significant wave height of 1.83 m and mean wave period of 5.19 s. We note that the turning wind conditions were well reproduced by the atmospheric model.

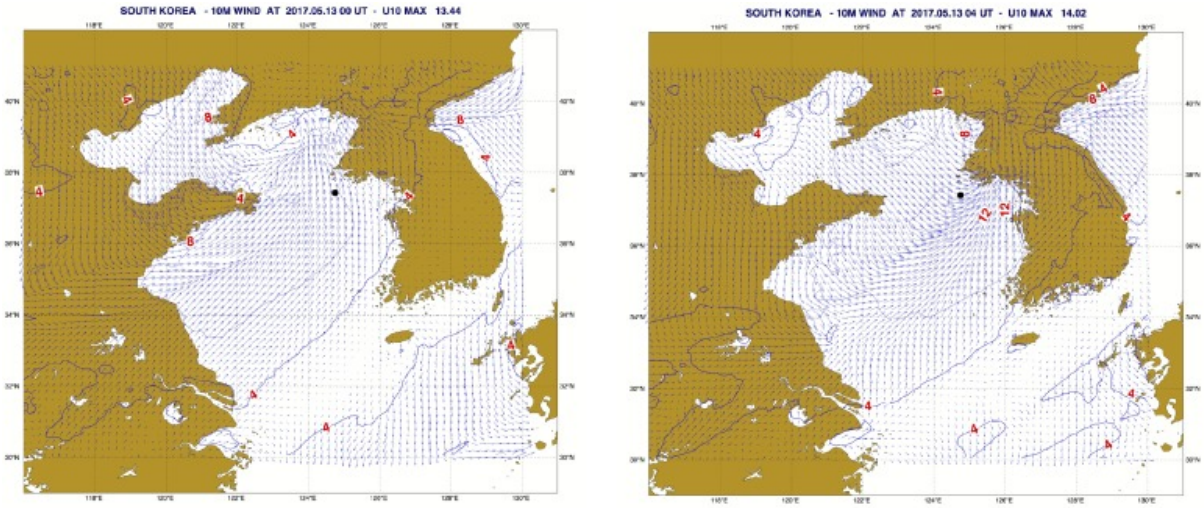

Fig. 4. Near-surface wind speed and direction (arrows) in the Yellow Sea on 13 May 2017, at 00 UTC (left panel) and 04 UTC (right panel), about the time when the cold front crossed the *Socheongcho-ORS* (shown on both panels with a black dot).

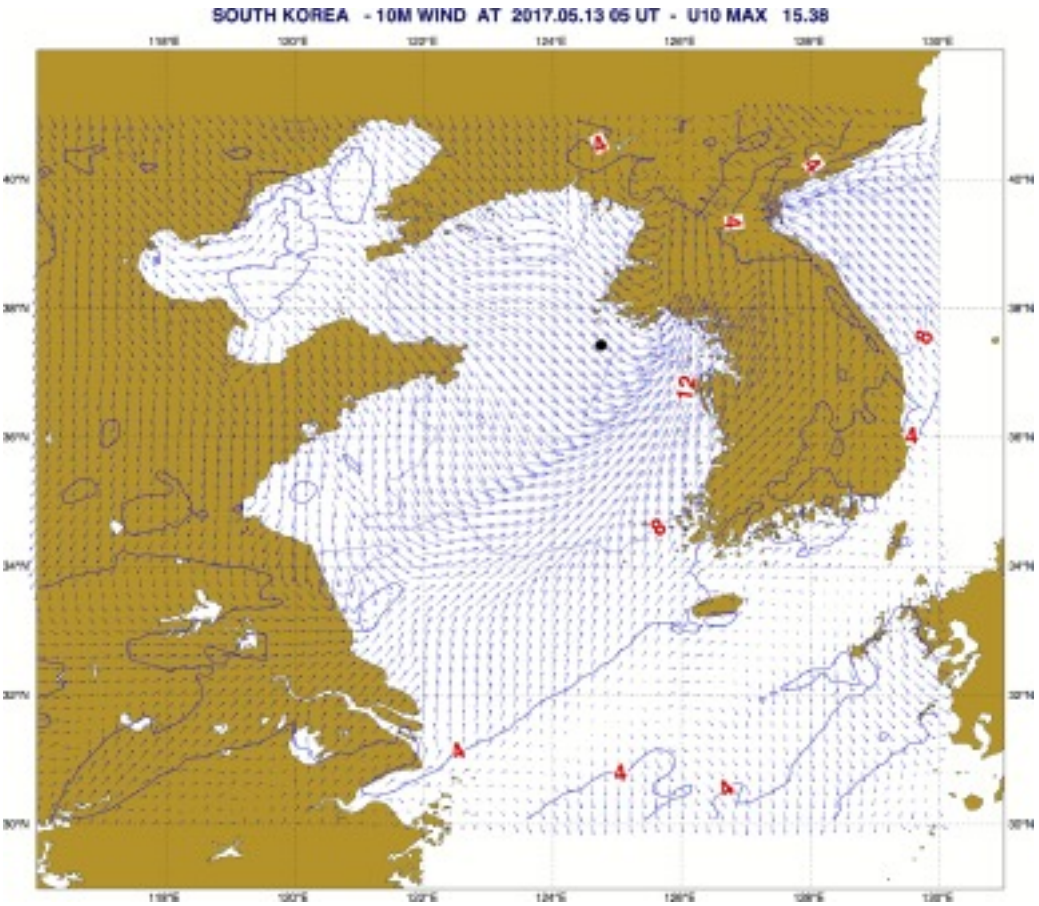

Fig. 5. Near-surface wind speed and direction (arrows) in the Yellow Sea on 13 May 2017, at 05 UTC, starting time of the WASS acquisition. The black dot shows the position of the *Socheongcho-ORS*.

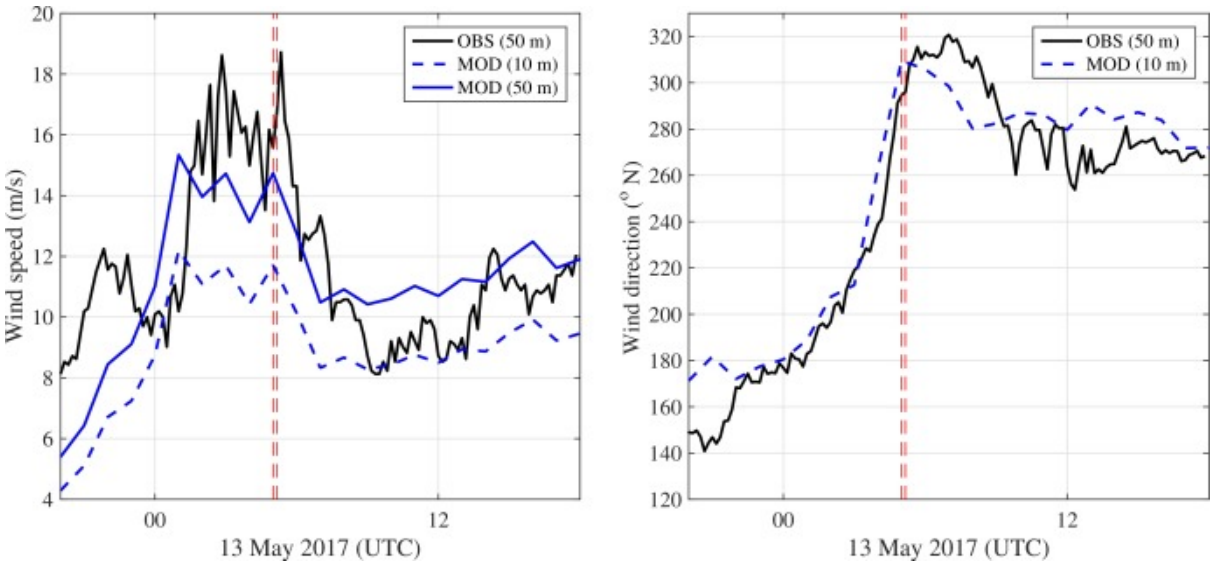

Fig. 6. Wind conditions at the *Socheongcho-ORS* on 13 May 2017. (left panel) Average wind speed recorded at 50-m height (OBS), modeled at 10-m height (MOD) and transformed to 50-m height wind speed assuming neutral stability conditions. (right panel) Mean wind direction (direction where the wind comes from, measured clockwise from geographic North). On both panels, the two vertical red dashed lines show the interval of the WASS acquisition, which started at 05 UTC.

At the position of the station, the turning winds following the front passage led to a new wave system from about 300° N superimposed to the pre-existing one (left panel of Fig. 7). As the result, the directional wave spectrum was now dominated by a coupled wind-sea swell system (Hasselmann et al., 1996). The old wind sea, carrying most of the variance of the sea state, was associated to the wave conditions before the passage of the front and was propagating from southwest, with peak frequency of 0.15 Hz and peak direction at 235° N, around which the spectrum is quite narrow in frequency (right panel of Fig. 7). In addition to this, the new wind sea from the northwest sector (270–310° N) produced a new peak (Fig. 7) and had a quite broad directional spectrum, both in frequency and direction, as typical of a more active sea under generative conditions. The presence of an isolated peak in the new wind direction seems to suggest that the change in wind direction was large and relatively fast (Young et al., 1987).

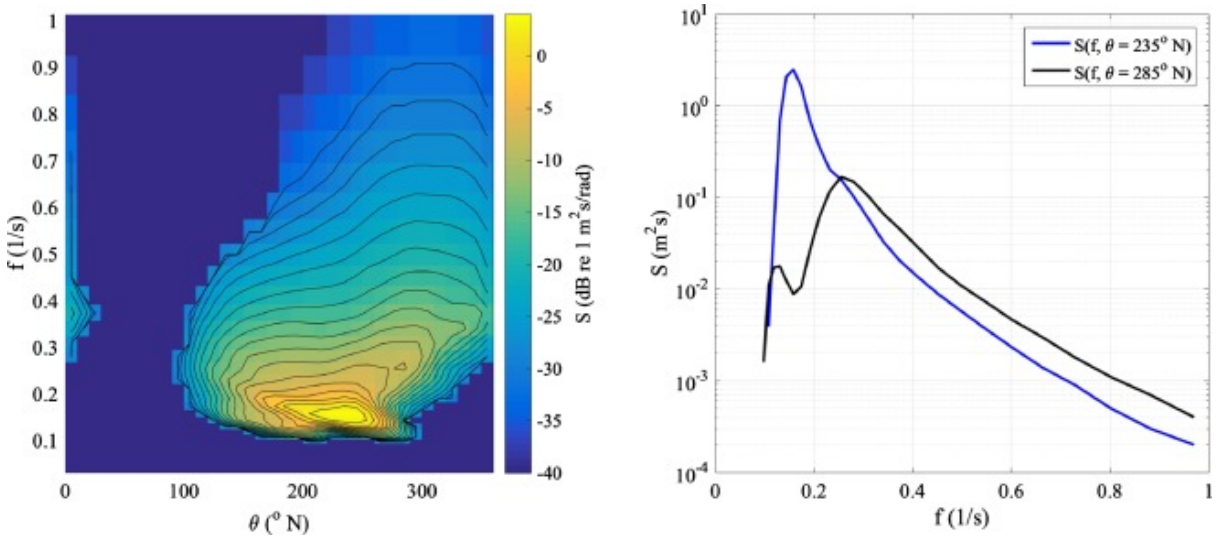

Fig. 7. (left panel) Frequency (f)-direction (θ) variance density spectrum $S(f, \theta)$ computed by the ECWAM model at the grid node closest to the position of the *Socheongcho-ORS* on 13 May 2017 at 05 UTC. The energy appears in the direction where it is coming from. Energy level isolines (solid black line) are shown at 2 dB interval. (right panel) Marginal frequency spectrum $S(f, \theta = \text{constant})$ at given directions $\theta = 235°$ N and $\theta = 285°$ N.

We shall discuss the directional properties of the observed wave field in the following sections. For the time being, we point out the two coupled wave systems in the WASS sequence. The first one (hereinafter W1, see left panel of Fig. 8), forced by the local wind, was seen propagating from the bottom-left of the images, approximately from northwest, while the second one (hereinafter W2, see right panel of Fig. 8), induced by the pre-existing wind conditions, was propagating from the bottom-right of the images, approximately from southwest.

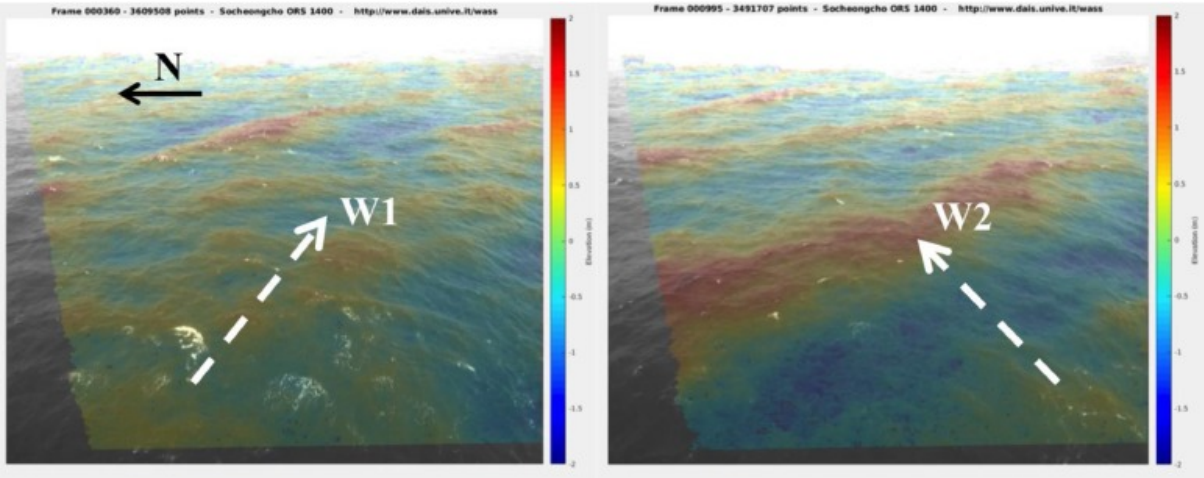

Fig. 8. The two principal wave systems at the *Socheongcho-ORS* on 13 May 2017 at 05 UTC. (left panel) The northwesterly system W1 (generative wind sea) is seen propagating from the bottom-left of the stereo images (note the active breaking along the direction of propagation of W1). (right panel) The southwesterly system W2 (pre-existing wave condition) is seen propagating from the bottom-right of the stereo images. On both panels, the sea surface elevation field (the colorscale is proportional to the value of z) is superimposed to the corresponding right stereo-image of WASS.

3. Characterization of the spatio-temporal wave field

The spatio-temporal sea surface elevation field $z(x, y, t)$ in the presence of waves is used to characterize the spectral and statistical properties of the wave field. The stochastic process z has variance σ^2 and it is assumed to be statistically homogeneous in the xy-space 2-D region Γ and stationary within the time interval.

3.1. Spectral domain

The representation of the physical space $z(x, y, t)$ with its variance density spectrum S is obtained via discrete N-Dimensional Fourier transform of the ST record. For typical stereo data, N might vary between 1 and 3. In this respect, the 3-D spectrum $S(k_x, k_y, \omega_a)$ is obtained from the 3-D Fourier transform pair that we write in the following vector form(1)Z(kx,ky,ωa)=∫t∫xz(x,y,t)ei(k·x−ωat)dxdtwhere $\boldsymbol{k} = (k_x, k_y) = (k\cos\theta, k\sin\theta)$ is the horizontal wavenumber vector of direction θ (computed clockwise from the positive direction of the k_y-axis), and $\omega_a = 2\pi f_a$ is the absolute angular frequency. Indeed, when a sea current is present, the distribution of wave energies in the 3-D spectral space is apparently shifted, since for a given wavenumber $\boldsymbol{k}$ the absolute wave frequency f_a seen by a fixed observer is different from the intrinsic (or relative) frequency f_i that would be measured by the same observer moving with the current. Indeed, the Doppler effect modifies the observed frequency of each elementary periodic wave that makes up the random sea (Lindgren et al., 1999). For harmonic waves in the limit of small wave steepness and neglecting the modulation of short waves by long waves (Longuet-Higgins and Stewart, 1960), the relation between f_a and f_i is given by the following formula (Stewart and Joy, 1974):(2)2πfa−2πfi−k·U=2πfa−2πfi−kUcos(θ−θU)=0where $\boldsymbol{U}$ is the medium velocity vector (of direction θ_U). At the leading order, it is assumed that the dispersion relationship of the linear wave theory provides a unique relationship

between the frequency f_i and the wavenumber k as follows:(3)ωi=2πfi=gktanh(kd)where ω_i is the intrinsic angular frequency, and g is the acceleration due to the gravity force. In general, the effective current $\boldsymbol{U}$ in Eq. (2) is a function of k, that is, $\boldsymbol{U} = \boldsymbol{U}(k)$, or, accordingly to Eq. (3), $\boldsymbol{U} = \boldsymbol{U}(f_i)$, since harmonic waves with wavenumber k can be considered to feel the current integrated from the surface up to the depth $\sim 1/k$ (Kirby and Chen, 1989, Stewart and Joy, 1974). Following Eq. (2), the spectral representation in absolute frequencies experiences a shifting of the energy distribution. In wave modeling this is used to estimate the local wave conditions. Here we work the other way around. We use the recorded k- and f_a-spectral information to evaluate the $\boldsymbol{U}$-vector (see Section 5). Once this is known, we map the 3-D Fourier components of $S(k_x, k_y, f_a)$ from the absolute frequency (k_x, k_y, f_a)-space to the intrinsic frequency (k_x, k_y, f_i)-space. For all wave modes of wavenumber $\boldsymbol{k}$, we may write(4)S(kx,ky,fi)=S(kx,ky,fa)Jaiwhere $J_{ai} = |df_a/df_i|$ is the Jacobian of the transformation, which in deep water can be written explicitly as(5)Jai=|1+(4π/g)fiUcos(θ−θU)|

For the data used here, the 3-D spectrum is estimated from the entire ST field $z(x, y, t)$ within an analysis window of area 93 × 109 m^2 (Fig. 9), which provides spectral resolutions $dk_x = 0.068$ rad/m, $dk_y = 0.058$ rad/m, and $df_a = 0.0017$ Hz. Before being Fourier transformed, to suppress the side-lobe leakage, the 3-D elevation data have been tapered with a Hanning window of the same size. It is worth noting that the 3-D spectrum has a high signal-to-noise ratio SN. If we define SN as the ratio between the energy at the spectral peak and the background energy away from the linear dispersion curve (Young et al., 1985), we find a background noise below −30 dB and values of SN in excess of 10000 (Figs. 10 and 11). Moreover, since the 3-D spectrum was obtained without any averaging over adjacent sub-records in either wavenumber space or frequency space (or both), the standard deviation of the spectral estimates are as large as the actual spectral values. This error is acceptable, since we use the 3-D spectrum to isolate the principal wave systems and to estimate the current vector (for which we only need a clear separation between the wave signal and the noise). Moreover, it can be shown (Jenkins and Watts, 1968) that the 2-D and 1-D spectra obtained by integrating the 3-D spectrum have a much smaller error of the spectral estimates. We note also that, in our case, the transformation in Eq. (4) is particularly prone to

errors for wave components longer than ~90 m that are not resolved within the analysis window AW (dashed black line in Fig. 13).

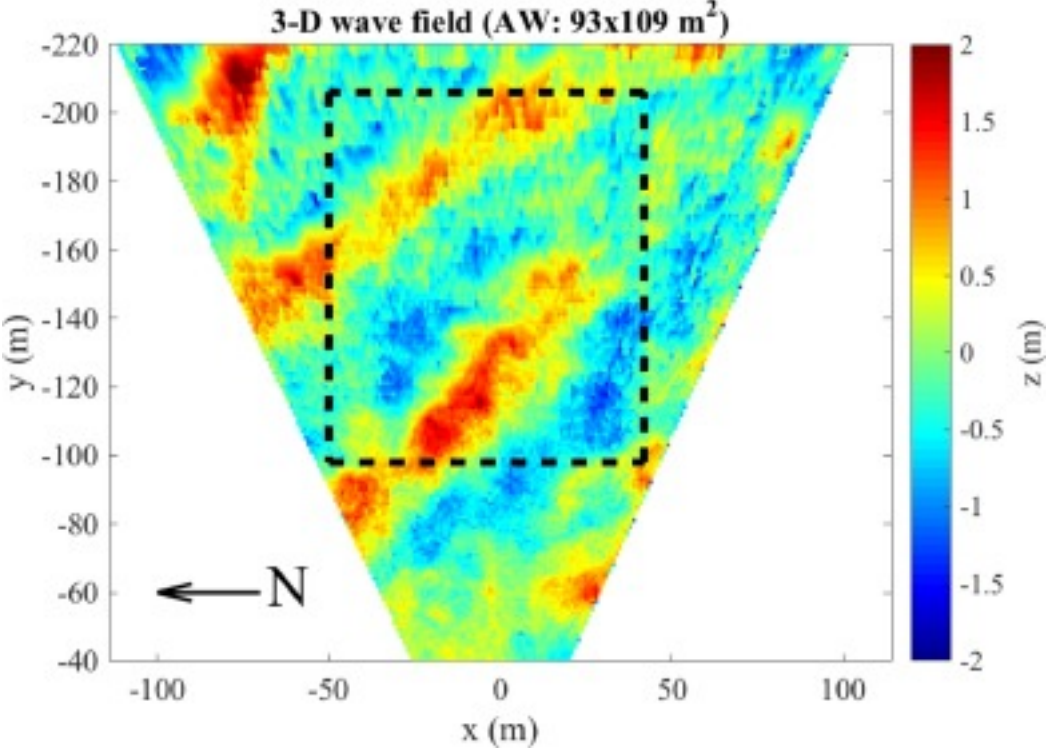

Fig. 9. Example of instantaneous 3-D wave field (x, y, z) observed with WASS. The dashed black rectangle delimits the analysis window (AW) used for the 3-D Fourier analysis of $z(x, y, t)$. The black arrow shows the direction of the geographical north (N) with respect to the camera axes.

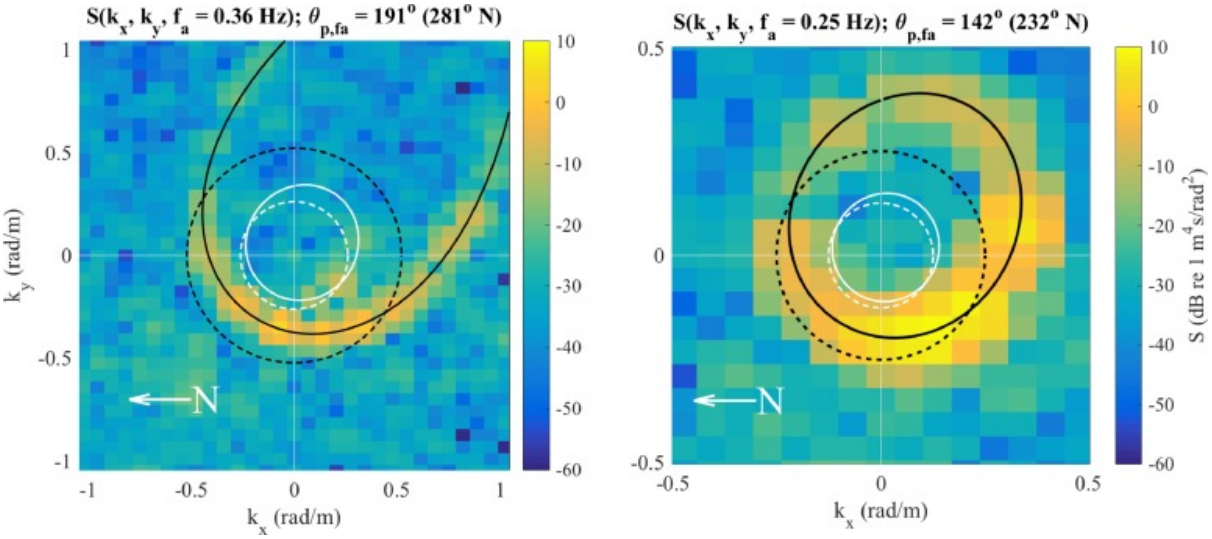

Fig. 10. 2-D section of the 3-D spectrum $S(k_x, k_y, f_a)$ at $f_a = 0.36$ Hz (left panel) and $f_a = 0.25$ Hz (right panel). The energy appears in the direction where it is coming from. Directions are computed clockwise from the positive k_y-axis. The dashed and solid black lines show the linear dispersion relation in still water and in presence of a uniform current, respectively. The dashed and solid white lines show the dispersion

relation of the positive interaction terms of the second-order nonlinear bound modes in still water and in presence of a uniform current, respectively. The axis limits change between panels for the sake of clarity. In each panel, $\theta_{p,fa}$ is the direction of the wavenumber where the 2-D marginal spectrum $S(k_x, k_y, f_a = \text{const.})$ is maximum. The white arrow shows the direction of the north (N) with respect to the camera x- and y-axis.

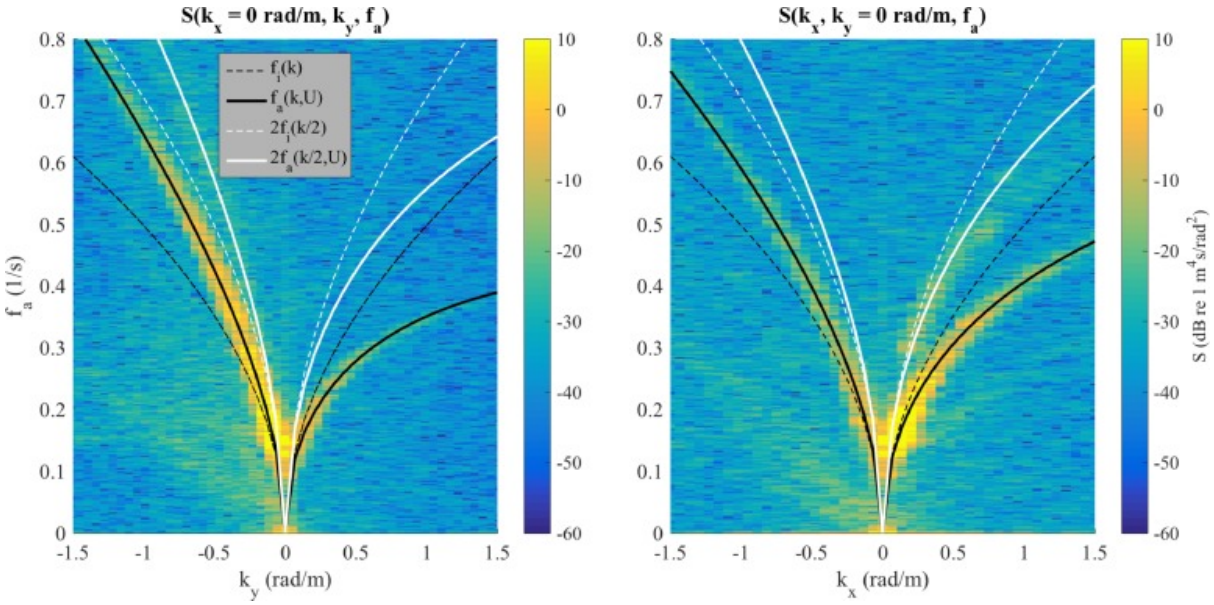

Fig. 11. 2-D section of the 3-D spectrum $S(k_x, k_y, f_a)$ at $k_x = 0$ rad/m (left panel) and at $k_y = 0$ rad/m (right panel). The energy appears in the direction where it is coming from. The dashed and solid black lines show the linear dispersion relation in still water and in presence of a uniform current, respectively. The dashed and solid white lines show the dispersion relation of the positive interaction terms of the second-order nonlinear bound modes in still water and in presence of a uniform current, respectively.

3.1.1. 3-D wavenumber/frequency spectrum

The contribution to the total variance σ^2 of the two principal wave systems W1 and W2 is visible by taking two sections in the (k_x, k_y)-plane of the full spectrum $S(k_x, k_y, f_a)$ at given frequencies $f_a = 0.36$ Hz (left panel of Fig. 10) and $f_a = 0.25$ Hz (right panel of Fig. 10). The apparent stretching of the linear dispersion relation due to the current (solid black line in both panels of Fig. 10) is more pronounced along its direction of propagation, which we estimate (see Section 5) approximately uniform at all frequencies and propagating, on average, at 1.13 m/s from 238° in the camera reference system (i.e., 328° N). The strong current-induced shift of the wave frequencies is also visible by taking two

sections in the wavenumber/frequency-plane of the full spectrum $S(k_x, k_y, f_a)$ at given wavenumbers $k_x = 0$ rad/m and $k_y = 0$ rad/m (Fig. 11).

The energy of the elevation field is mainly concentrated around the dispersion shell of free wave modes that we assume being described by the linear relation given in Eq. (3), even though a contribution is expected by nonlinear wave-wave interactions that redistribute energy among the free wave components (e.g. Janssen, 2009). Here, this contribution is neglected and the modification of the linear dispersion is associated solely to the current, which is therefore estimated accordingly. The 3-D spectrum shows also the variance of the positive interaction terms of the second-order nonlinear bound modes (Longuet-Higgins, 1963), whose energy, for a narrow spectrum and in presence of current, lies along the following dispersion curve(6)2πfa−2gk2tanh(k2d)−k·U=0which is plotted with a solid white line in Figs. 10 and 11. As expected, bound modes of the dominant wave system W2 are well distinct and rightly aligned with the direction of the peak (left panel of Fig. 10). Namely, we observe that the second-order nonlinear effects are dominant along the peak wave direction rapidly decaying in strength away from it. To empirically determine the significance of nonlinearities we have integrated separately the 3-D wave energy spectrum around the linear and second-order nonlinear dispersion shells. We have found the nonlinear modes stand a non-negligible fraction (about 5%) of the variance of free modes.

Although the 3-D spectrum provides considerable information about the wave field, it is more usual to present results in term of the 2-D directional spectrum or the 1-D frequency spectrum. In this respect, the 2-D wavenumber spectrum $S(k_x, k_y)$ holding the total energy of the sea state is obtained by integrating the 3-D spectrum $S(k_x, k_y, f_i)$ with respect to the intrinsic frequencies as follows:(7)S(kx,ky)=∫S(kx,ky,fi)dfi

The wavenumber/direction $S(k, \theta)$ spectrum in polar coordinates can be obtained by $S(k_x, k_y)$ using the following relationship:(8)S(k,θ)=S(kx,ky)Jwhere $J = k$ is the Jacobian used to transform the spectrum from the Cartesian (k_x, k_y)-domain to the polar (k, θ)-domain. The wavenumber and wavenumber/direction 2-D spectra are depicted in Fig. 12 and show, not surprisingly, that the largest amount of the wave energy is brought by the wave system W2, which has peak direction $\theta_p = 130°$, which corresponds to 220° N (consistent with the modeled spectrum in Fig. 7), and peak wavenumber $k_p = 0.09$ rad/m, about 1.4 times the spectral resolution. The

energy of the new wave system W1 is visible as a secondary lobe of the spectrum, which develops around 190° (280° N).

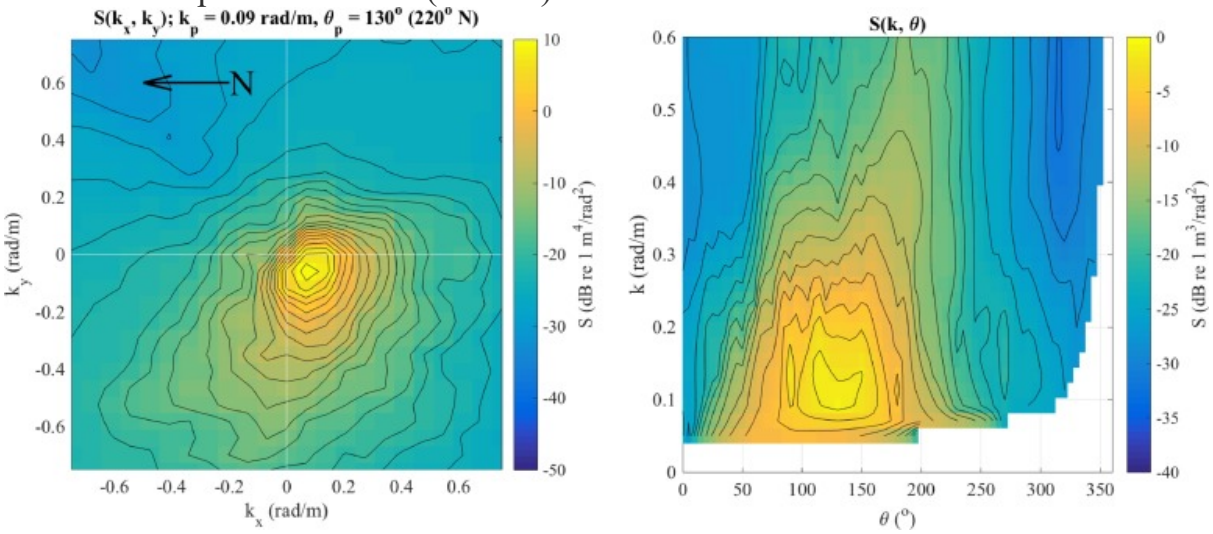

Fig. 12. (left panel) 2-D wavenumber spectrum $S(k_x, k_y)$. The energy appears in the direction where it is coming from. The arrow shows the direction of the geographical north with respect to the stereo camera axes. The direction of the peak of the spectrum is θ_p. (right panel) 2-D wavenumber-direction spectrum $S(k, \theta)$. On both panels, energy level isolines (solid black line) are shown at 2 dB interval.

3.1.2. 1-D frequency spectrum and directional distribution

For comparison with the modeled wave energy distribution, it is convenient to compute the omni-directional (i.e., integrated over all azimuth angles) frequency spectrum. Using the observed wave data, two frequency spectra can be retrieved by integration over wavenumbers of the 3-D spectrum in absolute frequency or intrinsic frequency, namely $S(k_x, k_y, f_a)$ and $S(k_x, k_y, f_i)$, respectively. That is,(9)S(fa)=∫∫S(kx,ky,fa)dkxdkyS(fi)=∫∫S(kx,ky,fi)dkxdky

The so derived absolute $S(f_a)$ and intrinsic frequency $S(f_i)$ spectra have a different shape, as it is shown in the left panel of Fig. 13. Despite the large frequency/direction spreading of the wave field, both spectra have a single peak, located at frequency $f_p = 0.15$ Hz (peak period $T_p = 6.7$ s), which corresponds to the dominant component of the old wind sea system W2. The peak wavelength L_p determined from T_p using the linear dispersion relation for gravity waves is 69 m. Comparing $S(f_a)$ and $S(f_i)$, we observe that the Doppler effect produces a frequency upshift of the short wave components of $S(f_a)$, mainly at frequencies higher than 0.45 Hz, which propagate with a linear phase speed of about 3.5 m/s (or less), about three times the current speed. We expect that the

waves carried by the new wind sea system W1 are the ones whose absolute frequency is mostly influenced by the current, since their direction of propagation is almost concurrent with the one of the current (see Fig. 10). For a Fourier component this implies that $f_a > f_i$. As a result, the two spectra $S(f_i)$ and $S(f_a)$ provide slightly different parameters of the sea state (within the integration range 0.0017 Hz - 0.7000 Hz): spectral significant wave height H_{m0} = (1.93 m, 1.93 m) for $S(f_i)$ and $S(f_a)$, respectively; average zero-crossing period T_z = (4.7 s, 4.6 s); average period T_{m01} = (5.0 s, 5.0 s); spectral bandwidth parameter (Longuet-Higgins, 1975) ν = (0.39, 0.43); mean spectral wave steepness (Fedele and Tayfun, 2009) μ = (0.060, 0.059).

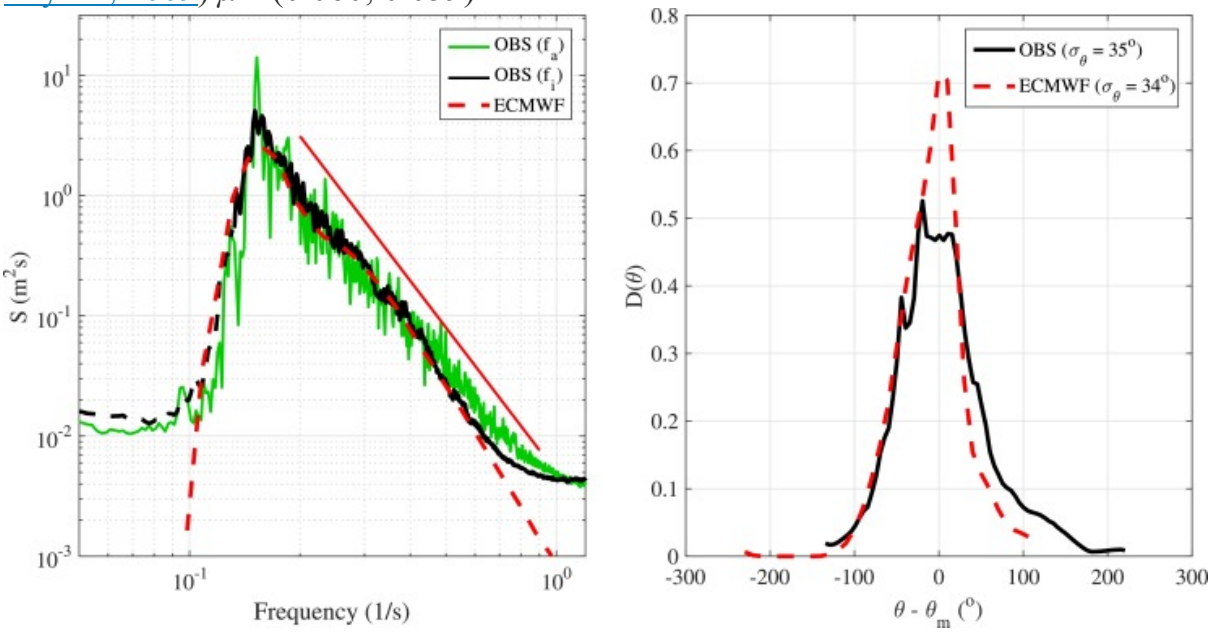

Fig. 13. (left panel) Observed (OBS) omni-directional frequency spectra $S(f_i)$ and $S(f_a)$ obtained from the 3-D spectra $S(k_x, k_y, f_i)$ and $S(k_x, k_y, f_a)$ by integration over all wavenumbers (k_x, k_y). Only the portion [0.05 Hz, 1.20 Hz] of the full spectral range [0.0017 Hz, 5 Hz] is shown. The spectrum $S(f_i)$ is shown with a dashed black line for the longer wave components that are not properly resolved in the 2-D (k_x, k_y)-spectral space. The modeled spectrum (ECMWF) is shown with a red dashed line. The red solid is the reference spectral slope proportional to f^{-4} (Phillips, 1985, Zakharov and Filonenko, 1967). (right panel) Integral directional distribution $D(\theta)$ of the observed (OBS) and model (ECMWF) directional spectra. For the sake of comparison, distributions are plotted against the relative direction θ–θ_m, where θ_m is the mean direction of each directional spectrum. In the legend, σ_θ is the directional spreading within the range θ–θ_m = [−90°, 90°], estimated following Holthuijsen (2007). (For interpretation of the references to color in this figure legend, the reader is referred to the web version of this article.)

The frequency spectra are used for a straight comparison with the numerical model computation. As it is visible in Fig. 13, in the high-frequency tail, the model spectrum (ECMWF) has energy levels consistent with those of $S(f_i)$, while it slightly underestimates the energy of the peak and the overall energy (the modeled H_{m0} is 1.77 m). This effect is possibly due to the underestimation of the modeled winds (Fig. 6), which is a long-standing issue of the global atmospheric model in semi-enclosed seas (see e.g. Cavaleri and Bertotti, 2004). The integral 1-D directional distribution $D(\theta)$ of the model spectrum is also assessed, and it is shown in the right panel of Fig. 13 for a comparison with the observed distribution. We note two different behaviors for the model $D(\theta)$: around the mean direction (close to the peak direction of the old wind sea system W2) the model spectrum width is comparable with the observed one, while it becomes narrower than observations for the new wind sea system W1 (visible as a secondary lobe at about 50° from the peak). The net effect is that the one-sided width σ_θ (directional spreading; Holthuijsen, 2007) of $D(\theta)$ is equal to 34° for the model spectrum, which is similar to the one derived from the observed spectrum ($\sigma_\theta = 35°$).

3.1.3. Number of 3-D waves

In this section, our goal is to estimate the average number of 3-D waves enclosed by the space region Γ and time interval D. To this end the spatial characteristics of the wave field are formulated in terms of spectral integral quantities, adapting the 1-D zero-crossing procedure (Rice, 1954) to 2-D spatial fields (Baxevani and Rychlik, 2004). In this respect, it is customary in the study of waves to consider as the lines for the spatial crossing the peak direction of wave propagation (θ_p), and the one perpendicular to it (θ_c), along the crests of the dominant waves. This coordinate system guarantees that the derivative along θ_p has larger variance than along θ_c, since the peak direction corresponds to that one of the vector with the largest eigenvalue of the covariance matrix of spatial derivatives (Baxevani and Rychlik, 2004). Hence, rotating around the origin the wavenumber spectrum $S(k_x, k_y)$ in order to align the x-direction with θ_p, we can evaluate the zero-crossing average wave (L_{zp}) and crest (L_{zc}) lengths in terms of the spectral moments as follows:(10)Lzp=2πm000m200;Lzc=2πm000m020where m_{abc} is the (a, b, c)th moment of the rotated wave spectrum $S_r(k_x, k_y)$ that we write as(11)mabc=∫∫kxakybficSr(kx,ky)dkxdky

Using Eqs. (10) and (11), we obtain $m_{200} > m_{020}$, and $L_{zp} = 31.1$ m and $L_{zc} = 38.5$ m. Since $L_{zc}/L_{zp} \sim 1$ the observed sea state is, on average, short-crested, as it is largely expected given the presence of wave systems crossing from different directions. However, since the low-wavenumber part of the spectrum is poorly resolved by the stereo system (see also Appendix A), both lengths L_{zc} and L_{zp} are expected to be underestimated.

Yet, being aware of this limitation, we use the characteristic lengths to evaluate the average number (N_{ST}) of 3-D waves within the ST region of volume $V = AD$. In analogy with the Rice's formula (Rice, 1954) holding for 1-D time records, and following the Euler Characteristic approach (Adler and Taylor, 2007), the value of N_{ST} can be expressed as (Baxevani and Rychlik, 2004, Fedele, 2012)(12)NST=VLzpLzcTz1+2αxtαxyαyt−αxt2−αxy2−αyt2where the coefficients α_{xy}, α_{xt} and α_{yt} in Eq. (12) originate from the cross-correlation coefficients of the sea surface gradients (at the limit of very “confused” sea state they all become zero). For the sea state considered here, $N_{ST} \approx 1200$, which will be used in Section 4 to estimate the probability of occurrence of rogue waves.

3.2. Statistical description

Here, statistical characteristics of the observed wave field are considered on a short-term scale. The variance σ^2 of the field $z = z(x, y, t)$ is readily estimated from the 3-D data as follows:(13)σ2=<(z−<z>)2>where the angle brackets < > denote the ensemble average. Because we have precautionarily pointed out (see Fig. 13 and Appendix A) that errors have an effect on observations above 0.7 Hz, for the determination of the statistical properties we have low-pass filtered at that frequency each time record $z(t)$ of the spatio-temporal field $z(x, y, t)$. Moreover, since the accuracy is not uniform within the region Γ, the statistical analysis is limited to wave data in the range up to 210 m from the station. In this range, from filtered data, we have computed the standard deviation $\sigma = 0.486$ m and estimated the significant wave height as $H_s \approx 4\sigma = 1.94$ m.

3.2.1. Distribution of ST sea surface elevations

In Section 3.1.1, we have observed that the 3-D wave spectrum shows two principal modes, which represent the variance of free and nonlinear bound waves. Although we have shown that bound modes are less energetic than free modes (see also Tayfun, 1990), the former have a fundamental role in shaping sea surface

elevation fields, producing waves with high sharp crests and shallow rounded troughs (Longuet-Higgins, 1963).

The contribution to non-Gaussianity due to bound harmonics is manifest in a non-zero skewness (m_3) and contribution to the excess kurtosis ($m_4 - 3$) of the distribution of sea surface elevation (Longuet-Higgins, 1963), that we estimate from the ST field using the following formulae:(14)m3=<(z−<z>σ)3>,m4=<(z−<z>σ)4>

For our measurements we obtain $m_3 = 0.14$ and $m_4 = 3.10$, which indeed indicate a departure of the process from the Gaussianity. This effect is visible in Fig. 14, where the histogram of the observed (OBS) elevations $z(x, y, t)$ is compared with the Gaussian probability density function (GAU) and nonlinear extensions (GC3 and GC4) that account for the coefficients of skewness and kurtosis, respectively (Longuet-Higgins, 1963), which well approximate the empirical distribution

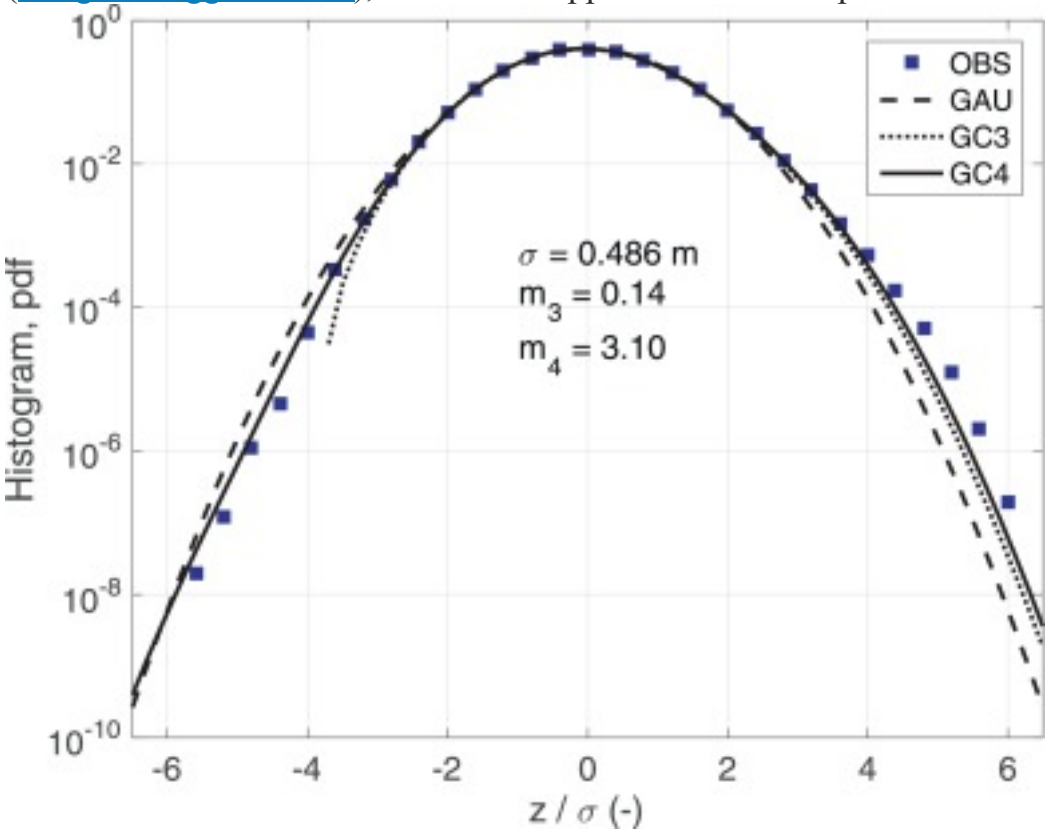

Fig. 14. Histogram of the normalized observed surface elevations (OBS). Theoretical curves: Gaussian (GAU) probability density function (pdf), and non-Gaussian pdfs that account for m_3 (GC3) and m_3 and m_4 (CG4).

3.2.2. Spatial, temporal and spatio-temporal length scales

In this section, we examine the characteristic length scales of the ST wave field. Results are mostly based on the analysis of the shape of the autocovariance

function (λ), whose use we extend to determine the temporal coherence of the spatial fields.

At first, analyzing the 2-D spatial field $z(x, y)$, an indication of the spatial coherence of the wave field is given by the shape of the autocovariance function computed along specific directions of $z(x, y)$. We have then selected 1-D spatial transects of $z(x, y)$ along the two orthogonal directions: the normal-to-crest direction θ_p (that we denote with the coordinate X), and the along-crest direction θ_c (coordinate Y). The normalized autocovariance functions are then computed as

follows:(15)λp(Δ)=<z(X)z(X+Δ)><z(X)z(X)>λc(Δ)=<z(Y)z(Y+Δ)><z(Y)z(Y)>where Δ is the discrete spatial lag. Since the lag (Δ_{min}) of the first minimum of λ approximates (Boccotti, 2000) the mean distance between the wave crest apex (attained at $\Delta = 0$) and the closest trough, using the functions in Eq. (15) we obtain an estimate of the wave and crest lengths of the highest waves in each 2-D field. Then, averaging the profiles of λ_p and λ_c over the whole time sequence of data permits to evaluate the average length scales of the dominant waves along θ_p and θ_c. As it seen in Fig. 15, the two functions λ_p and λ_c decay with different gradients from the maximum, clearly showing that the typical scales along the peak direction are smaller (the first zero-level is crossed at a lower lag and $\Delta_{min} = 27$ m) than the ones along the wave crests ($\Delta_{min} = 61$ m).

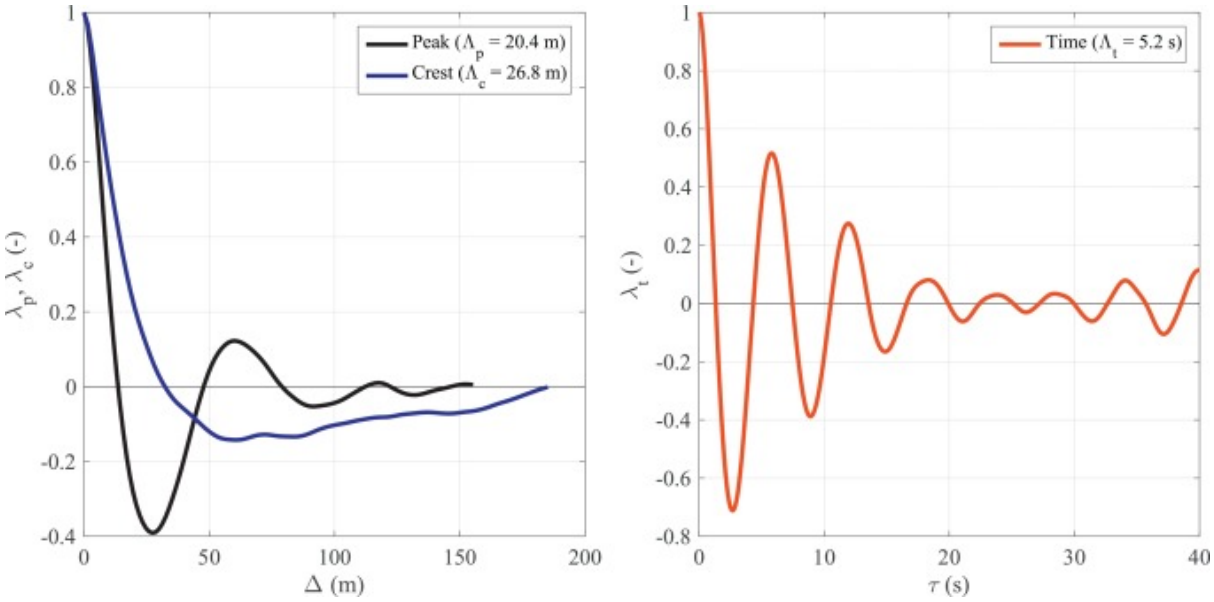

Fig. 15. (left panel) Normalized spatial autocovariance functions along the peak direction of wave propagation (θ_p) and the direction of the wave crests (θ_c). The spatial lag is Δ. (right panel) Normalized temporal autocovariance function. The time lag is τ. In both panels, the legend shows the integral length scale of the process.

The correlation distances of the process are measured by the integral length scales, which look at the overall “memory” of the process and for wave fields are given by (Zavadsky et al., 2017)(16)Λp=∫|λp(Δ)|dΔΛc=∫|λc(Δ)|dΔalong the peak and crest directions, respectively. The two integral lengths are $\Lambda_p = 20.4$ m and $\Lambda_c = 26.8$ m, approximately 0.65 times the average lengths L_{zc} and L_{zp} along the consistent directions, and about 0.3–0.4 times the peak wavelength L_p. These empirical estimates are consistent with the ones reported by Zavadsky et al., (2017) in their experiments in a wind-wave tank, who also showed that the ratios Λ_p / L_p and Λ_c / L_p decrease with fetch and wind velocity. For the data analyzed in this study, we note that, given the limited sea surface region covered by the stereo system, the covariance functions do not attain zero at the maximum distance, which implies that the two length scales (16) are probably slightly underestimated.

The temporal scales are determined adopting a similar procedure. To this end, the temporal autocovariance function λ_t (right panel of Fig. 15) of the time series of sea surface elevation $z(t)$ at the mid-point of the sea surface region Γ is computed as(17)λt(τ)=<z(t)z(t+τ)><z(t)z(t)>where τ is the discrete time lag. The first minimum of λ_t is attained at $\tau = 2.7$ s, which would provide a period of the highest waves of 5.4 s, smaller than T_p, consistent with the principles of the Quasi-Determinism (QD) model by Boccotti (2000). The integral time scale(18)Λt=∫|λt(τ)|dτis equal to 5.2 s, which implies that, on average, the sea surface elevation temporal profile loses memory of the overall process after about one mean wave period.

The determination of the temporal memory of the 2-D spatial fields $z(x, y)$ requires a different strategy. In this case, we are interested in verifying the coherence between the fields $z(x, y)$ at different instants, accounting for the wavenumber dispersion, which is the primary physical mechanism connecting spatial and temporal scales of wind waves. Therefore, it is natural, at first, to compute the dependency using the cross-correlation coefficient (CC) between an initial field at time $t = t_0$, namely $z(x, y, t = t_0)$, with $(x, y) \in \Gamma$, and the one at time $t = t_0 + \tau$, where τ is a time lag larger than zero. Following this approach, we observe (left panel of Fig. 16) that CC decreases rapidly with τ, up to a first minimum on average at $\tau = 2.8$ s, when the 2-D fields are approximately in counter-phase. This value of τ is close to the corresponding one yielded by λ_t (Fig. 15). The reason for this similar fashion is that the CC is mostly influenced by the dominant waves, which are the ones characterized also by the temporal autocovariance function. Thus, this approach for estimating the coherence between fields $z(x, y)$ simply

conveys the dynamics of the highest waves of the sea state and tells little about the role of the wave dispersion.

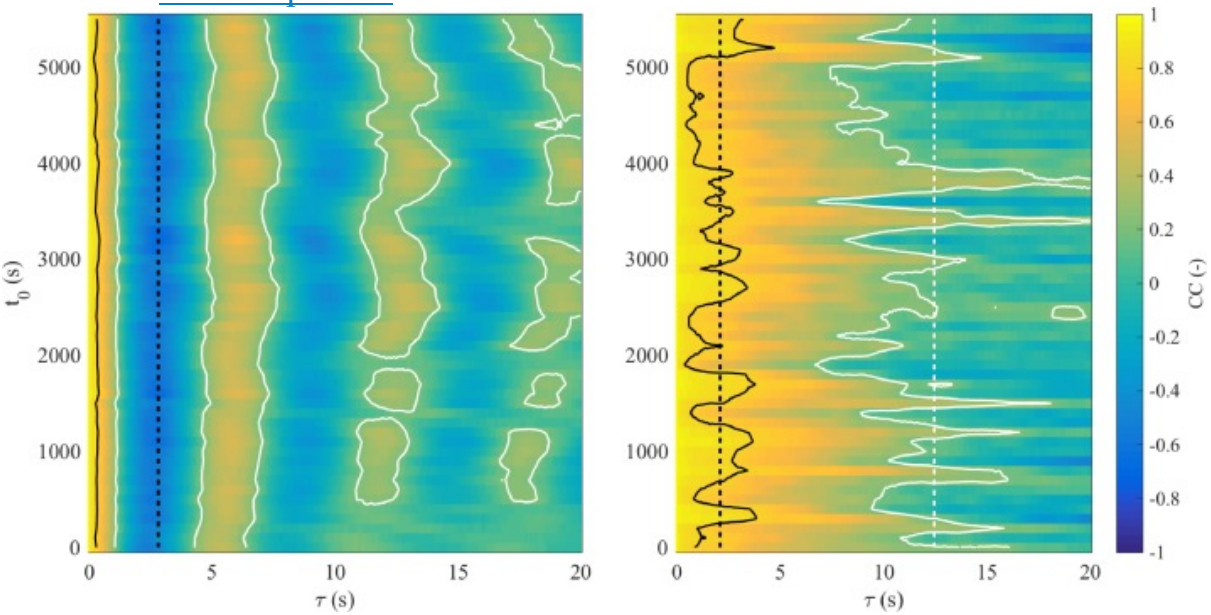

Fig. 16. Temporal coherence of spatial 2-D fields. (left panel) For each time $t = t_0$, the map shows the cross-correlation coefficient CC between the observed field $z(x, y)$ at the time lag τ and the one at $\tau = 0$. The vertical dashed black line corresponds to the average lag of the first minimum of CC. The black solid line shows the level $CC = 0.8$, and the white solid line shows the level $CC = 0.2$. (right panel) For each time $t = t_0$, the map shows the cross-correlation coefficient CC between the observed field $z(x, y)$ at the time lag τ and the one predicted at τ using the phase-shifted 2-D Fourier Transform of the field $z(x, y)$ at $\tau = 0$. The black solid line shows the level $CC = 0.8$, and the white solid line shows the level $CC = 0.2$. The vertical black dashed line shows the average lag $\tau = 2.1$ s of the level $CC = 0.8$, while the vertical white dashed line shows the average lag $\tau = 12.5$ s of the level $CC = 0.2$.

We have thus adopted an alternative method to evaluate the coherence, proceeding as follows. At a certain time $t = t_0$ we have computed the instantaneous wavenumber spectrum $S_0(k_x, k_y)$ of the 2-D field $z(x, y, t = t_0)$ within the analysis window shown in Fig. 9. For each wavenumber $\boldsymbol{k} = (k_x, k_y)$, the 2-D spectrum $S\tau(k_x, k_y)$ at the lagged time $(t_0 + \tau)$ has been estimated by linearly shifting the Fourier phases. Leaving unchanged the spectral amplitudes and inverting back from the spectral to the spatial domain, we obtain a prediction $z^*(x, y, t = t_0 + \tau)$ of the actual wave field $z(x, y, t = t_0 + \tau)$ at $t_0 + \tau$ (Fig. 17). Then, by computing CC between z and z^* we can assess the memory of the spatial fields, i.e. for how long the dispersive spatial wave field remains coherent. The result is shown on the right panel of Fig. 16. In this case, we observe a large variability

of *CC*, depending mainly on the average size of the waves that are delimited by the region Γ at time $t = t_0$. The *CC* levels 0.8 and 0.2 are reached, on average, after 2.1 s and 12.5 s, respectively, and the correlation drops to zero after about 15 s. The average value of the integral spatio-temporal scale Λ_{ST} estimated from the *CC* field is 6.6 s, i.e., after this time interval the wave dispersion is not able anymore to describe the elevation field, since new wave packets are entering the region Γ, while others are leaving it. We note that Λ_{ST} is larger than Λ_t and assumes a value close to T_p.

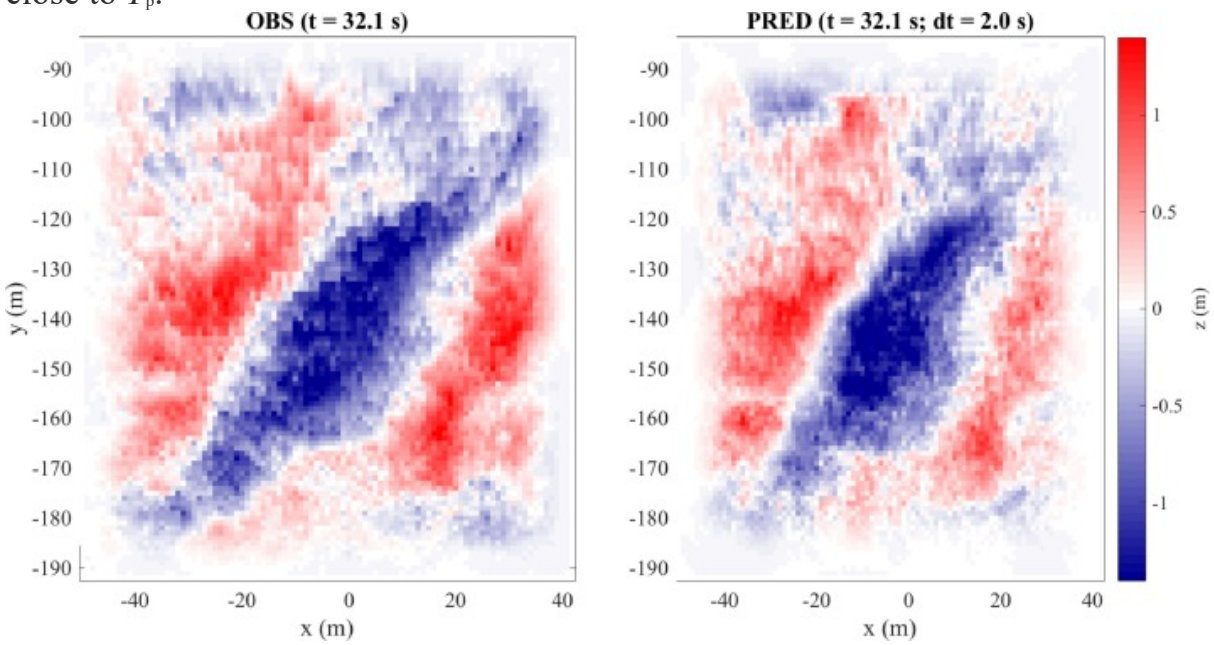

Fig. 17. Example of observed wave field *z* (OBS; left panel) and predicted *z** (PRED; right panel) by linear shifting the Fourier phase of d*t* = 2.0 s.

4. Spatio-temporal properties of rogue waves

Ocean wave observatories relying on instruments capable of measuring the spatio-temporal sea surface elevation field are gaining consensus for being appropriate to observe rogue waves, which appear as an erratic 3-D phenomenon that can occur at any time and location of the sea surface (Benetazzo et al., 2017a, Donelan and Magnusson, 2017). In this respect, recent studies (Benetazzo et al., 2015, Schwendeman and Thomson, 2017) have shown that stereo wave imaging systems provide an effective blend of accuracy and spatial coverage which makes such instruments profitable in the field of extreme wave measurements. Indeed, it was proven (Benetazzo et al., 2017b, Fedele et al., 2013) that observing for ~30 min a 2-D sea surface region with sides larger than the characteristic wave and

crest length (say L_{zc} and L_{zp}), the expected value of the maximum wave crest height exceeds $1.25H_s$, that is, one of the classical criterions to define whether or not an individual wave is a rogue wave (Draper, 1964, Dysthe et al., 2008).

4.1. Exceedance distribution of rogue waves

In this study, to look for rogue waves within the ST record $z(x, y, t)$, we have followed the same approach as adopted by Benetazzo et al. (2015), and hence we have split the sea surface region Γ and the time interval D in adjacent and non-overlapping subrecords. Here, we choose sixteen ST regions V_s (with $s = 1, 2, \ldots, 16$) of equal area $A_s \approx 5400$ m^2 and duration $D_s = 150$ s, in order to produce independent realizations of the random variable "maximum crest height" defined as follows:(19)zm=max{z(x,y,t)|(x,y,t)∈Vs}
The statistical independence of these realizations was verified checking that maxima were not belonging to the same wave group. The crest heights so obtained range between 2.08 m and 2.92 m, and their exceedance distribution is shown in Fig. 18, where the values of z_m are normalized with the standard deviation σ.

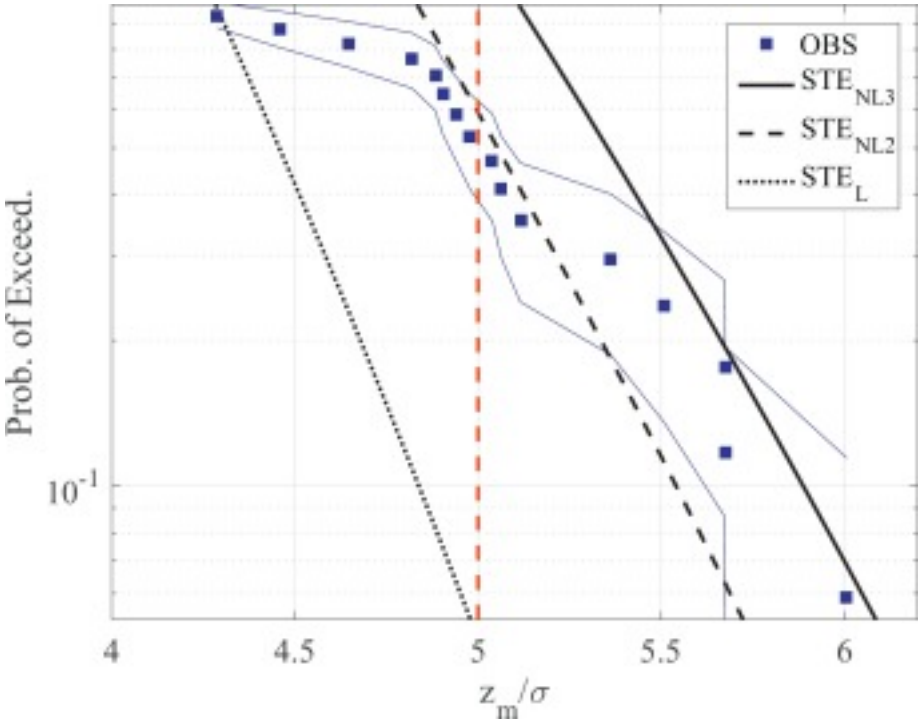

Fig. 18. Probability of exceedance of normalized extreme crest heights. Observations (OBS) and relative upper and lower stability bands (blue line). STE_{NL3} is the asymptotic extreme value distribution of third-order nonlinear maximum crest heights (Fedele et al., 2017); STE_{NL2} is the second-order model (Benetazzo et al., 2015); STE_L is the Gaussian (linear) model (Fedele, 2012). The vertical red dashed line is the

rogue wave threshold $z_m = 1.25H_s = 5\sigma$. (For interpretation of the references to color in this figure legend, the reader is referred to the web version of this article.)

The empirical exceedance distribution is used to assess the stochastic model for the asymptotic prediction of space-time extremes in Gaussian seas (STE_L in Fig. 18; Adler, 2000, Fedele, 2012), and its extensions that include the contributions from second-order bound harmonics (STE_{NL2} Fig. 18; Benetazzo et al., 2015) and further third-order bound harmonics and quasi-resonant wave-wave interactions (STE_{NL3} in Fig. 18; Fedele et al., 2017). For large values of the threshold, the third-order nonlinear probability is here approximated as follows:(20)Pr{zm>ξσ|Vs}≈[2πNVs(η2−1)exp(−η2/2)+(Pr2D+Pr1D)][1+(Λ/64)η2(η2−4)] where $N_{Vs} = N_{ST}/16$ is the average number of 3-D waves enclosed by V_s, and η and ξ are the normalized (with σ) linear and second-order nonlinear elevation thresholds, respectively, which satisfy the Tayfun (1980) quadratic equation(21)ξ=η+μ2η2→η=−1+1+2μξμ
The parameter Λ is a measure of third-order nonlinearities and is a function of the fourth-order joint cumulants of the sea surface elevation and its Hilbert transform (Tayfun and Fedele, 2007). In our study, Λ is approximated in terms of the excess kurtosis as $\Lambda = 8/3\ (m_4 - 3)$, which strictly holds for long-crested waves. The two additional terms Pr_{2D} and Pr_{1D} in Eq. (20) are the boundary corrections which accounts for the possibility that extremes "touch" the boundaries of the ST region (Fedele, 2012, Fedele et al., 2013). The fair agreement in Fig. 18 between the third-order nonlinear and the empirical probabilities of the highest crests conveys the fundamental role of bound nonlinearities (that we expect mostly contribute to the excess kurtosis; Fedele et al., 2017) in the formation of high and eventually rogue waves (Benetazzo et al., 2017b, Benetazzo et al., 2015, Donelan and Magnusson, 2017, Fedele et al., 2016, Gemmrich and Thomson, 2017). Elaborating this point further, we note that out of the sixteen values of z_m, eight exceed $1.25H_s$ (Fig. 18) and thus they can be classified as belonging to rogue waves. The crest height z_m and the crest-to-trough wave height H_m for these waves are reported in Table 1. Compared to the average number N_{ST} of waves within the ST volume, we find that a wave whose crest height exceeds the threshold $1.25H_s$ occurs on average once every $\sim 10^2$ waves. This probability of occurrence is consistent with recent empirical estimations of the likelihood of rogue waves in space and time (Benetazzo et al., 2017a), and it is between one and two orders of

magnitude larger than the probability of encountering rogue waves in single-point time observations (Christou and Ewans, 2014, Gemmrich and Thomson, 2017).

Table 1. Parameters of the individual rogue waves and their average values (Avg): z_m/H_S is the normalized crest height, H_m/H_S is the normalized crest-to-trough wave height.

Rogue wave	**1**	**2**	**3**	**4**	**5**	**6**	**7**	**8**	**Avg**
z_m/H_s	1.26	1.27	1.28	1.34	1.38	1.42	1.42	1.50	1.36
H_m/H_s	1.71	1.95	2.04	2.18	1.97	2.02	2.09	2.39	2.05

4.2. Size of rogue waves

In this section, we address additional aspects of the rogue waves such as the extension of the sea surface region they actually span. An indication of the size of the sea surface region where the elevation z exceeds $1.25H_s$ can be derived analytically, following the approach originally developed by Longuet-Higgins (1957) for a random, moving, Gaussian surface. This author derived, for a given total surface area A_{tot}, the expected value l_c of the length of the contour bounding the region exceeding a linear threshold elevation (say η) as a function of the spectral moments. That is,(22)lc{(x,y)∈Γ:z(x,y)>ησ}=Atotπm200+m020m000exp(−η22)f(γ)where $f(\gamma)$ is an elliptic integral ranging between 1.0000 and 1.1107 for long- and short-crested waves, respectively. For non-Gaussian surfaces, to account for the effect of second-order bound nonlinearities that enhance crest heights, we propose (similarly to the approach presented for the length of crests by Romero and Melville, 2011) to modify Eq. (22) using the nonlinear distribution by Tayfun given in Eq. (21). Hence, the linear elevation η is replaced with the second-order nonlinear elevation ξ, and the second-order nonlinear approximation $l_{c,NL}$ of l_c is computed as(23)lc,NL{(x,y)∈Γ:z(x,y)>ξσ}=Atotπm200+m020m000exp(−η22)f(γ)where for rogue wave characterization we assume $\xi = 5$. For the data presented in this study, and using $A_{tot} = A$, we find $l_{c,NL} = 0.12$ m, which is a small value compared to the typical length scales of waves. However, Eq. (23) does not provide any estimate of the area spanned by rogue waves, when they occur. In order to obtain that estimate we must rely on observations, as we show below.

Two examples of what the observed 3-D shape $z_{RW} = z(x, y)$ of a rogue wave looks like are presented in Fig. 19: rogue waves appear as isolated crests, whose

transversal extension is limited by the directional spreading of waves that bounds the crest length. To quantify the area of the horizontal surface surrounding the rogue waves, we have averaged the fields z_{RW} in order to obtain an estimation of the characteristic 3-D shape of rogue waves. The result is shown on the left panel of Fig. 20, where the values of z have been divided by H_s. Clearly, the average shape of the highest waves is stretched along the direction of the crests of the wave system W2: the distance between the crossings of the levels $z = 0$ is about 80 m. The 3-D profile is narrower along the peak direction, with distance of 27 m between the crossing the levels $z = 0$; this distance would provide a wavelength of the highest waves of 54 m, smaller than L_p, consistent with the results of the QD model.

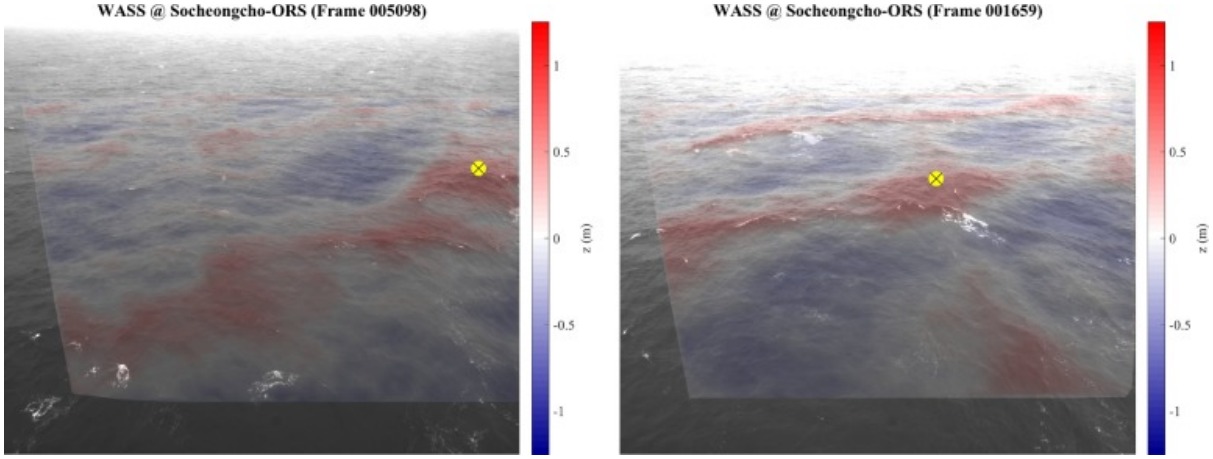

Fig. 19. Examples of rogue waves observed at the *Socheongcho-ORS*. On both panels, the sea surface elevation field (the colorscale is proportional to the value of z) is superimposed to the grayscale image acquired by the left stereo-camera of WASS. The yellow dot shows the position of $\max\{z(x, y)\}$.

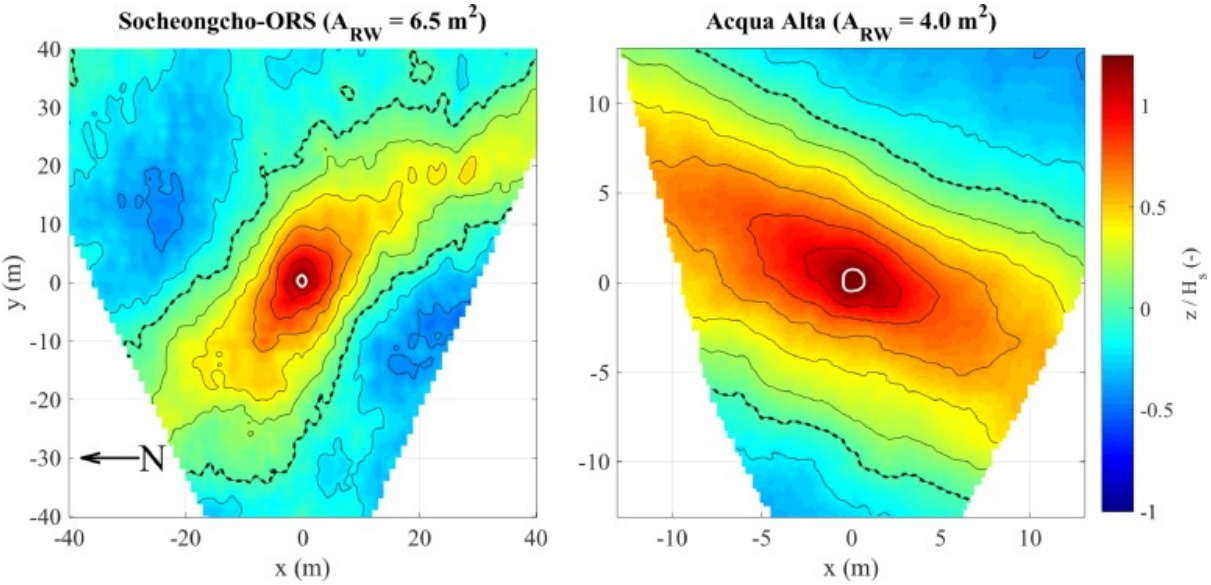

Fig. 20. Average shape of the normalized (with H_s) sea surface elevation field $z(x, y)$ at the time of the rogue waves collected within the spatio-temporal record. (left panel) WASS data collected at the *Socheongcho-ORS*. Only the rogue waves (5 out of 8) occurring close to the center of the observed region were used. The arrow shows the direction of the geographical north with respect to the stereo camera axes. The dashed thick line shows the level $z = 0$, and the inner white contour shows the isoline $z = 1.25H_s$. The average area of the sea surface where $z > 1.25H_s$ is A_{RW}. (right panel) As on the left panel, but for WASS data collected at the *Acqua Alta* oceanographic research platform (Benetazzo et al., 2015). On both panels, $\max\{z(x, y)\}$ is set at the position $(x, y) = (0, 0)$ and surface elevation isolines (solid black line) are shown at 0.2 interval.

The excursion set Γ_{RW}, defined as the portion of the observed region Γ where the sea surface elevations meet the threshold criterion $z > 1.25H_s$, has a small extent: indeed, for the rogue waves presented in this study the mean area A_{RW} is about 6.5 m^2, that is, $A_{RW} \sim (10^{-2}–10^{-3})L_{zc}L_{zp}$. Assuming for simplicity that Γ_{RW} is circular, the radius of A_{RW} would be 1.44 m. For comparison, rogue waves collected with a stereo system installed on the oceanographic research platform *Acqua Alta*, Italy (details in Benetazzo et al., 2015) have a similar shape (right panel of Fig. 20) and a slightly smaller extent, being in this case the average value of $A_{RW} = 4.0$ m^2. Once normalized with the severity of the sea state, in both cases, the area $A_{RW} \sim 2Hs2$. Further, the spatio-temporal wave data permit also direct estimates of the temporal profile of the eight rogue waves, which are reported on the left panel of Fig. 21, while on the right panel of the same Figure, the profile of the wave with the maximum crest height is compared with that one of the iconic Draupner rogue wave (Haver, 2004, Magnusson and Donelan, 2013), and of the highest wave

within a similar ST record gathered at the *Acqua Alta* platform (Benetazzo et al., 2015). We observe that all rogue waves, either collected in the same sea state or in different sea conditions, have similar shape, in particular for sea surface elevations around the maximum. This is consistent with the prediction of the Slepian Model Representation (Lindgren, 1972) or the QD theory and it further confirms recent experimental results in open sea conditions (Benetazzo et al., 2017a).

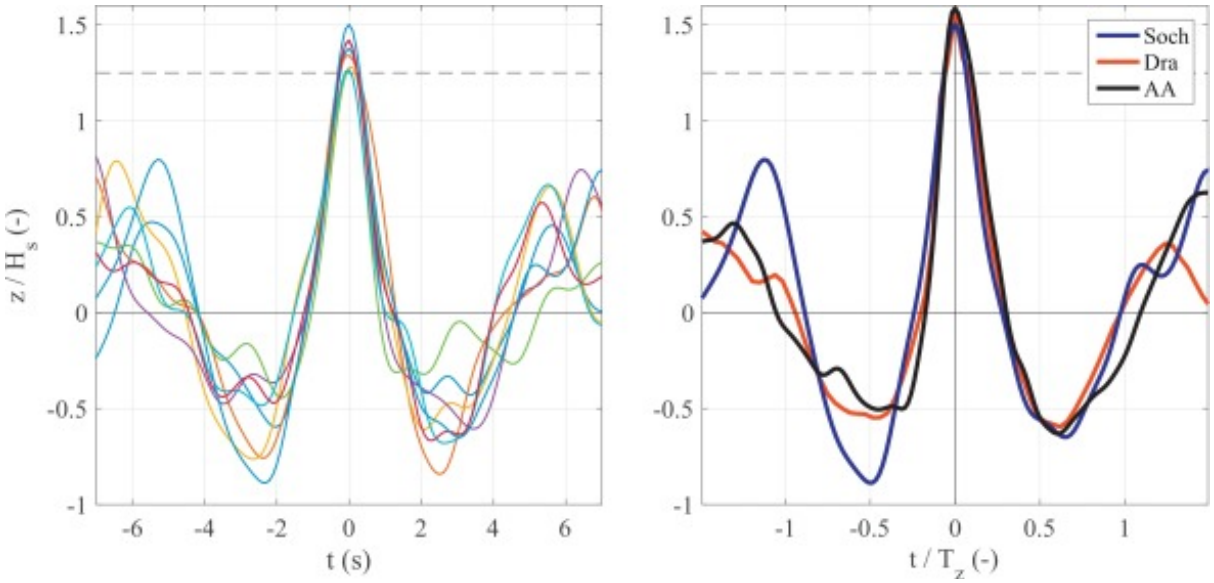

Fig. 21. (left panel) Temporal profile of the normalized (with H_s) sea surface elevation around the eight rogue waves observed at the *Socheongcho-ORS*. The time of the maximum elevation is set equal to zero for all profiles. The horizontal dashed gray line at 1.25 represents the rogue threshold. (right panel) Temporal profile of the normalized (with H_s and T_z) sea surface elevation around the largest rogue wave observed at *Socheongcho-ORS* (Soch). The Draupner (Dra) rogue wave is shown with red solid line, while the largest rogue wave (AA; see Benetazzo et al., 2015) collected at the platform *Acqua Alta* is shown with black solid line. (For interpretation of the references to color in this figure legend, the reader is referred to the web version of this article.)

5. Estimate of the near-surface current velocity

As it has been previously assessed by Benetazzo et al. (2012), the 3-D wave spectrum $S(k_x, k_y, f_a)$ produced using WASS data has enough spectral resolution and high signal-to-noise ratio to give a good estimate of the sea current vector at possibly different depths. Similarly to what is commonly performed with marine radars (Senet et al., 2001, Serafino et al., 2010, Young et al., 1985), this estimate is carried out by comparing the actual wave energy distribution with the linear

dispersion shell we have previously described in Eq. (3). Practically speaking, once we choose a given wave frequency f_t (i.e. we take a 2-D section of the 3-D spectrum $S(k_x, k_y, f_a)$, slicing at $f_a = f_t$ the wavenumber domain $(k_x, k_y) \in \Omega \subseteq \Re^2$; see for instance Fig. 10), we obtain a curve Ψ defined as the set of all the points $\boldsymbol{k} \in \Omega$ for which:(24)$$\lambda(k)=g\|k\|\tanh(\|k\|d)+k\cdot U-2\pi ft=0$$
Since we expect that most of the energy of $S(k_x, k_y, f_a = f_t)$ is located around Ψ, we can estimate the optimal current $\boldsymbol{U}$-vector so that the curve integral of $S(k_x, k_y, f_a = f_t)$ along Ψ is maximized. Unfortunately, the numerical computation of such an integral is difficult in practice for two reasons. First, the curve Ψ exhibits a behavior that makes it difficult to obtain an explicit representation of its equation. Second, since we only know $S(k_x, k_y, f_a = f_t)$ on a regular grid of discrete samples, we would face the non-trivial problem of correctly interpolating S (in presence of noise) along a discretized version of the curve. Hence, the common approaches used to estimate $\boldsymbol{U}$ are based either on a sparse fitting of the curve in least-square sense (Senet et al., 2001), or by manually tuning the current vector so that Ψ visually overlaps the high energy regions of the spectrum. Both the approaches have drawbacks. The former requires a thresholding of the spectrum to identify high-energy point candidates on which the curve is fitted. The latter is essentially a graphical approach that is subject to human intervention.
Our proposed method exploits the fact that $\gamma(\boldsymbol{k})$ is the zero level-set of the curve Ψ. Indeed, Ψ is defined implicitly by all the points for which $\gamma(\boldsymbol{k}) = 0$, which have the additional property of being positive for the points outside of the curve and negative inside. Hence, we can transform the curve integral along Ψ to a spatial integration on the whole domain Ω by combining $\gamma(\boldsymbol{k})$ with the following Dirac delta function:(25)$$\int\Psi S(s,ft)=\int\Omega\delta[\gamma(k)]S(k,ft)dk$$
In this setting, we can pose the estimation of the sea current at a temporal frequency f_t as the following unconstrained minimization:(26)$$\operatorname{argmax}U\in\Re 2\int\Omega\delta[\gamma(k)]S(k,ft)dk$$
Having transformed the optimization in a form in which we don't need to integrate over the curve, we can deal with the real case scenario in which we only have a discrete sampling of S possibly affected by noise. We start by considering the following Gaussian approximation of δ(27)$$G(x)=e-x2/\beta$$where β is a scale factor. We then multiply $\gamma(\boldsymbol{k})$ with the inverse of $\|\nabla\gamma(\boldsymbol{k})\|$, so that the value at each point $\boldsymbol{k}$ varies with a unitary rate with the distance from the zero level set, and we discretize (26) as

follows:(28)argmaxU∈ℜ2∑(kx,ky)G(γ(kx,ky)‖∇γ(kx,ky)‖)S(kx,ky,ft)∑(kx,ky)G(γ(kx,ky)‖∇γ(kx,ky)‖)where (k_x, k_y) span over the discrete range of wavenumbers recovered in the 3-D spatio-temporal spectrum.

To clarify the approach, in Fig. 22 we have plotted the value of G(γ(kx,ky)‖∇γ(kx,ky)‖) for different values of f_t and β. Essentially, β acts as a smooth integration mask which is maximum along Ψ and decreases when moving away from the curve with a rate depending by β. Increasing β has a similar effect as smoothing S with a low-pass Gaussian filter and helps reducing the noise. On the other hand, a small value of β improves the localization of the curve and increments the accuracy of the estimation. Depending on the quality of the spectrum S, one can favor the robustness of the estimation against noise or the accuracy of the recovered sea current. Finally, the normalization factor ∑(kx,ky)G(γ(kx,ky)/‖∇γ(kx,ky)‖) has been added so that the integral of the mask over the integration domain is unitary. This is needed, otherwise the optimization will naturally favor longer curves regardless the values of S.

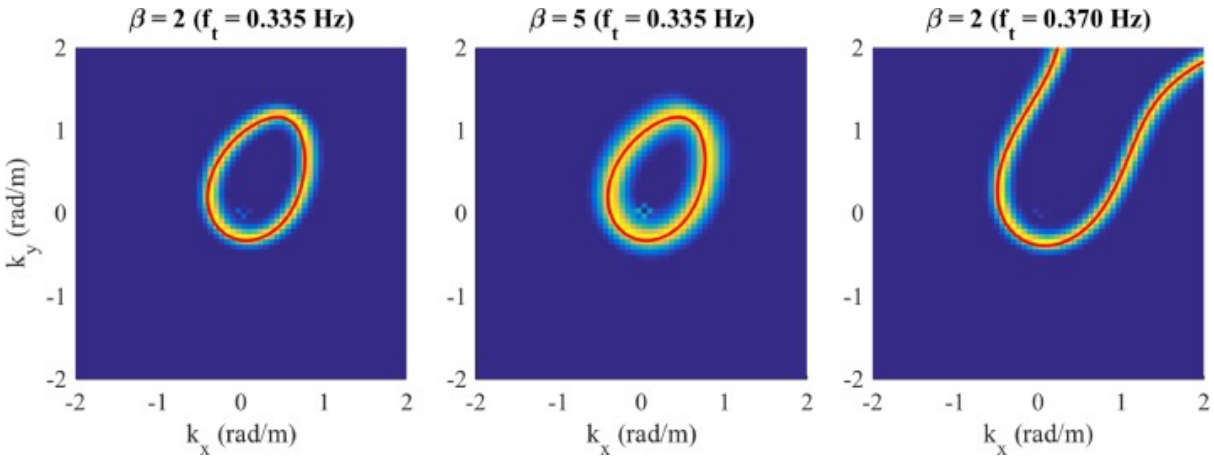

Fig. 22. Examples of the function G(γ(kx,ky)‖∇γ(kx,ky)‖) computed at the frequency $f_a = f_t$ for different values of β. $U = (-0.5$ m/s, -1.0 m/s). The parameter β is directly proportional to the width of the integration band centered along the curve Ψ which has been superimposed in red for visualization.

We have applied the proposed method to the wave data collected from *Socheongcho-ORS* for different values of the frequency f_t ranging from 0.2009 Hz to 0.6837 Hz. To correct the nonlinear nature of the spectral response, in Eq. (28) we substituted $S(k_x, k_y, f_a = f_t)$ with $-\log[S(k_x, k_y, f_a = f_t)]$, and transformed accordingly the maximization to a minimization. We used the Matlab® function *fminsearch* to solve the problem numerically, starting from an initial

guess of $\boldsymbol{U} = (-0.6\ \text{m/s}, -1.02\ \text{m/s})$ which have been empirically determined. In all the runs of our algorithm, we use the same value of $\beta = 1$ and iterated until the norm of $\boldsymbol{U}$ between two subsequent steps was lower than $TolX = 10^{-8}$ (usually after a hundred iterations).

In Fig. 23 we have plotted the current speed U and direction θ_U for different values of the frequency f_a. From the data we can observe that the modest directional resolution of the 3-D wave spectrum at frequencies less than about 0.3 Hz partially limits the capability to retrieve a robust estimation of the current vector (indeed, sharp variability is seen in the values of U and θ_U). On the contrary, for frequencies above 0.35 Hz, the current vector shows almost constant values of U and θ_U, that we estimate, on average, equal to $U = 1.13$ m/s and $\theta_U = 238°$ (328° N). We interpret the small dependence of the current on the wave frequency as the consequence that it was mainly tidal driven rather than forced by the wind. Unfortunately, independent measurements of the current profile at the *Socheongcho-ORS* during the WASS deployment were not available.

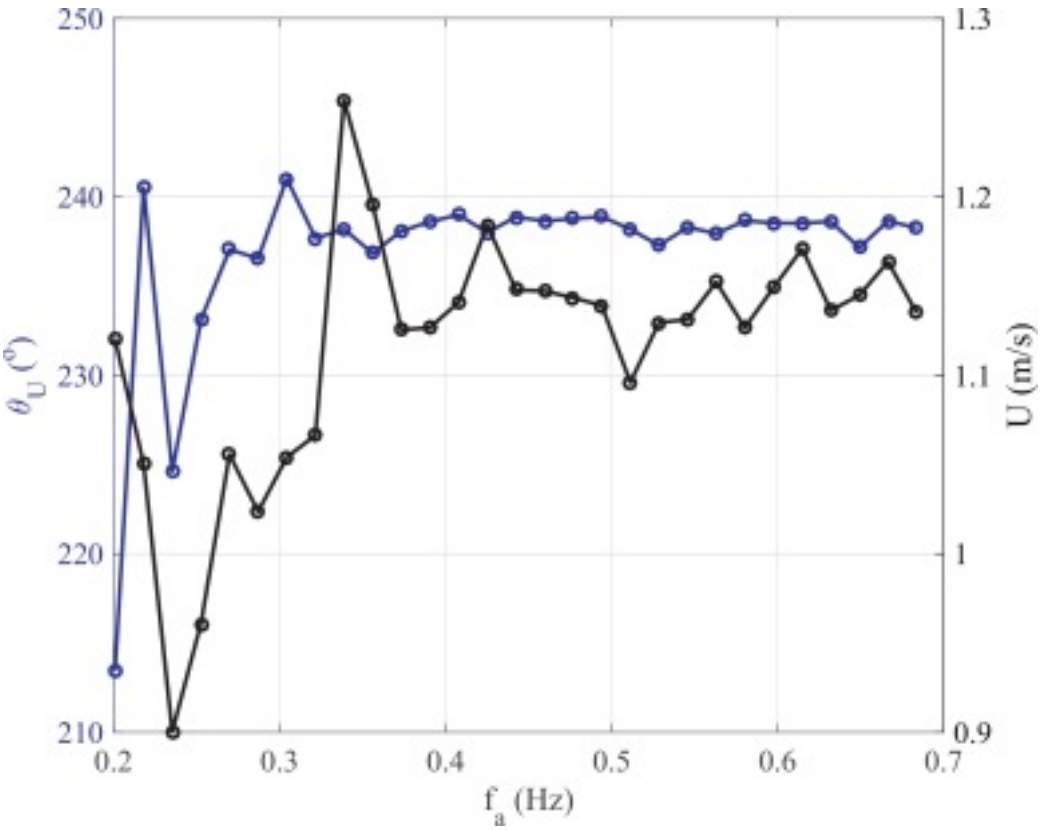

Fig. 23. Current velocity (U) and direction (θ_U) estimated from WASS data for different frequencies at the *Socheongcho-ORS* on 13 May 2017 at 05 UTC. The current incoming direction is computed clockwise from the positive camera y-axis.

However, an historical characterization of the sea currents at that station was done in November 2016 by deploying an acoustic current doppler profiler (ADCP). The ADCP data show (Fig. 24) that the current spectrum is dominated by semi-diurnal tides, which have a tidal ellipse with principal axis oriented northwest-southeast, and speed along that direction that exceeds 1 m/s, with minor variations from the sea surface through the bottom (not shown here). This behavior is consistent with the historical simulations of the tidal currents in the Yellow Sea made by Yanagi and Inoue (1994) and with recent model evaluations (courtesy of Dr. Yonggang Wang of the First Institute of Oceanography, Qingdao, China, 2017, personal communication).

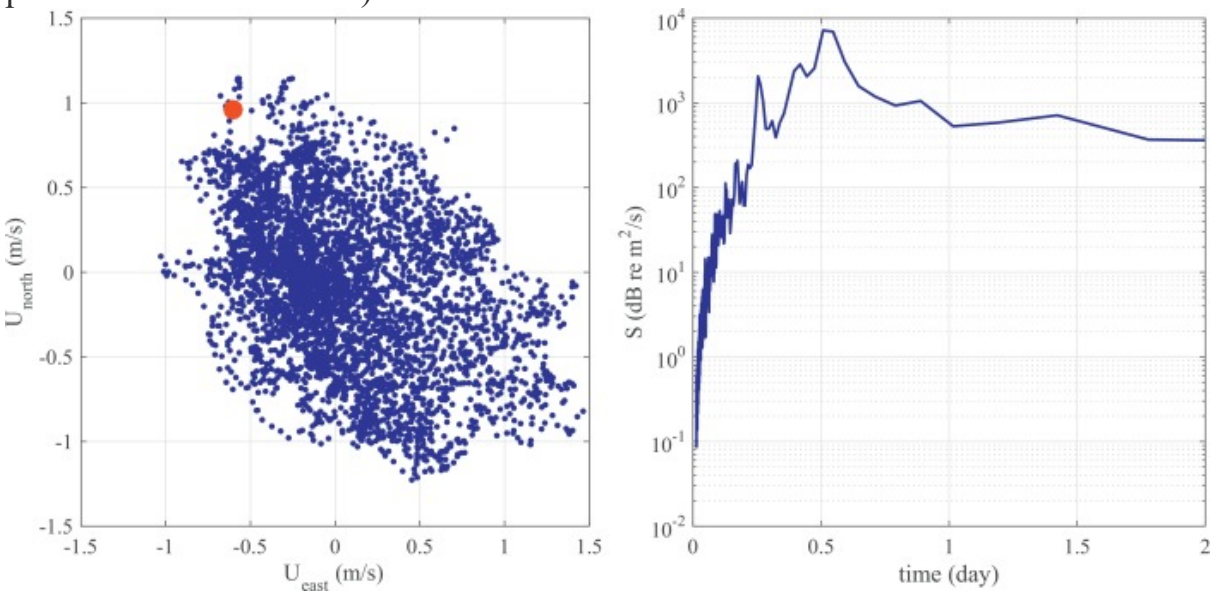

Fig. 24. (left panel) North and south components of the surface current velocity vector *U* measured at the *Socheongcho-ORS* on 1–30 November 2016 using an ADCP (blue dotes), and average current measured with WASS on 13 May 2017 at 05 UTC (red dot). (right panel) Variance density spectrum of the surface current speed *U* measured with the ADCP. (For interpretation of the references to color in this figure legend, the reader is referred to the web version of this article.)

6. Conclusions

In this study we have empirically characterized the distinctive signature of a spatio-temporal sea surface elevation field. Open ocean wave data were acquired in the Yellow Sea with a stereo imaging system that provided a time sequence of 3-D wave fields, whose spectral and statistical features were analyzed. The principal conclusions of our study can be summarized as follows:

•Spatio-temporal sea surface elevation fields provide the most complete source of information for wind wave analysis and interpretation presently available. Here, we have used these data to show the wavenumber/frequency spectral response of the wave field during the rapid passage of an atmospheric front. This led to a large spreading of the wave energy, eventually producing a mixed wind sea-swell condition, whose main systems were isolated in the observed 3-D wave spectrum.
•The two coupled wave systems were also fairly reproduced by a modeled spectrum (from ECWAM), which has a directional distribution consistent with the observed one, but it underestimates the wave energy near the spectral peak, most likely because of the weak intensities of the modeled winds.
•We argue that care must be used in interpreting frequency wave spectra in presence of strong sea currents. Indeed, we have shown that the mapping in absolute frequencies distorts the shape of the energy distribution and can lead to an erroneous evaluation of integral wave parameters, which can be important, for instance, in the assessment of wave model performances.
•The length scales of the wave process have been characterized using the spatial and temporal autocovariance functions. The correlation distance of the wave field has been measured by the integral scales that have highlighted the contribution of average and dominant waves, as well as, for the spatial fields, of the wave dispersion.
•As it has been already suggested in previous studies, rogue waves are more numerous and likely in spatio-temporal wave fields than in time wave records. Here this finding has been confirmed during a mixed sea condition, which we judge can lead to large occurrences of high waves. In this respect, we have shown that in this condition the occurrence probability of rogue waves is well approximated by the prediction of a stochastic model for spatio-temporal nonlinear wave extremes.
•Further, we have empirically estimated the area of the 2-D sea surface region bounded by a rogue wave. The mean coverage is in the order of one percent of the area spanned by the average wave and crest lengths, and this clearly compounds the problem of measuring rogue waves with single-point instruments.
•The *Socheongcho-ORS* resulted a favorable site for wave-current interactions studies, being the tidal currents as large as 1 m/s. In this paper the Doppler shift of the wave energy in the 3-D spectrum was used to determine the sea current vector using a novel and effective strategy. The proposed method is not

only applicable to stereo wave data, but also to any other instrument able to provide ST wave fields, such as marine wave radars.
The prospect for future investigations includes additional campaigns in the Yellow Sea to broaden the experimental results and improve the knowledge of the local extreme wave conditions, including typhoons.

Acknowledgments

This research was supported by the project "Construction of Ocean Research Stations and their Application Studies", funded by the Ministry of Oceans and Fisheries, Republic of Korea. We are grateful for the efforts of the reviewers whose insights greatly improved this paper. Luigi Cavaleri and Luciana Berotti have been partially supported by the EU contract 730030 call H2020-EO-20116 'CEASELESS'.

Appendix A. Analysis of the errors of the sterero system

In this Appendix, we analyze the principal sources of error associated with the stereo wave imaging technique. Two main causes of uncertainties can be expected for any stereo method: the uncertainty in the recovery of the 3-D coordinates (quantization error), and the uncertainty in the determination of the corresponding pixels for each image pair (matching error). Indeed, when designing a stereo-camera system one must compromise between accurate 3-D estimation and reliable image feature-matching. In fact, as pointed out by Mironov et al. (2012), the major difference between stereo wave imaging and the classical problem of stereo reconstruction is in the fact that the water surface reflectance is not Lambertian. However, Benetazzo (2006) shown that the matching error is small for highly-textured water surfaces, and Jähne (1993) indicated that the matching error is small when the wave slope is much larger than the inclination of the stereo cameras optical axis. For the installation at the *Socheongcho-ORS*, the geometry of the stereo rig was empirically tuned so that the interplay between the light vector, the point of view and the surface normal is similar for the two cameras. Thus, we can assume that the disparity of each corresponding pixel is dominated by the spatial position of the 3-D surface point and not by the rather complex water surface bidirectional reflectance distribution function.

To provide an accurate 3-D reconstruction, particular care has to be taken when choosing the imaging system parameters, the main ones being the pixel cell size and numbers (i.e. the camera resolution), the focal length, the baseline, the camera reciprocal orientation, and the distance from the stereo-camera system to the scene of interest. Under general conditions, in order to keep small the range error due to quantization (hence to provide high accuracy in the 3D reconstruction) the baseline-to-distance ratio must be large. However, accurate feature points matching requires this ratio to be small (Jähne, 1993, Rodriguez and Aggarwal, 1990). An optimal set-up must be found. Based on our experience on stereo wave imaging at the sea (Benetazzo, 2006, Benetazzo et al., 2016, Benetazzo et al., 2015, Benetazzo et al., 2012), the correspondence problem is negligible, in absence of sun glitters, setting stereo cameras with optical axes (almost) parallel in order to reduce as small as possible the angle between them, and letting the average baseline-to-distance as small as possible (around 0.10). For our tests this ratio was around 0.04.
What remains to quantify is the quantization error; indeed because of the discrete nature of the image formation system, the image coordinates of each pixel can suffer from quantization errors up to 1/2 pixel. Therefore the disparity can be in error as much as 1 pixel. Because of this error, the estimation of the range along the optical axis is inexact, as well along the two directions orthogonal to it. The error along the optical axis dominates (Benetazzo, 2006, Jähne et al., 1994, Rodriguez and Aggarwal, 1990). The quantization error is alleviated by using subpixel (fractional pixel) correspondence, which reduces errors depending on the weight function adopted to estimate the cross-correlation map (Nobach and Honkanen, 2005), and it has a large impact on the accuracy of the smaller wavelengths (Benetazzo et al., 2012).
Using the geometry of the WASS installation at the *Socheongcho-ORS*, the quantization error distribution was quantified via 3-D reconstruction of an arbitrary wavy surface mapped onto the imaged area. The difference between the actual 3-D surface and that one retrieved after applying the stereo method is shown on the left panel of Fig. 25. We observe that, as expected, errors increase with the distance from the cameras, particularly along the y-axis, and have a maximum absolute value of about 10 cm, with a root-mean-square error of 3 cm, assuming a factor of 5 as a conservative upper bound for sub-pixel improvement (Benetazzo et al., 2016). The characteristic amplitude and wavelength of the vertical errors are shown in the right panel of Fig. 25, from where we can infer that the maximum errors, expected at the furthest distance, have length $L_{\mathrm{err}} \approx 7$ m and amplitude $a_{\mathrm{err}} \approx 10$ cm.

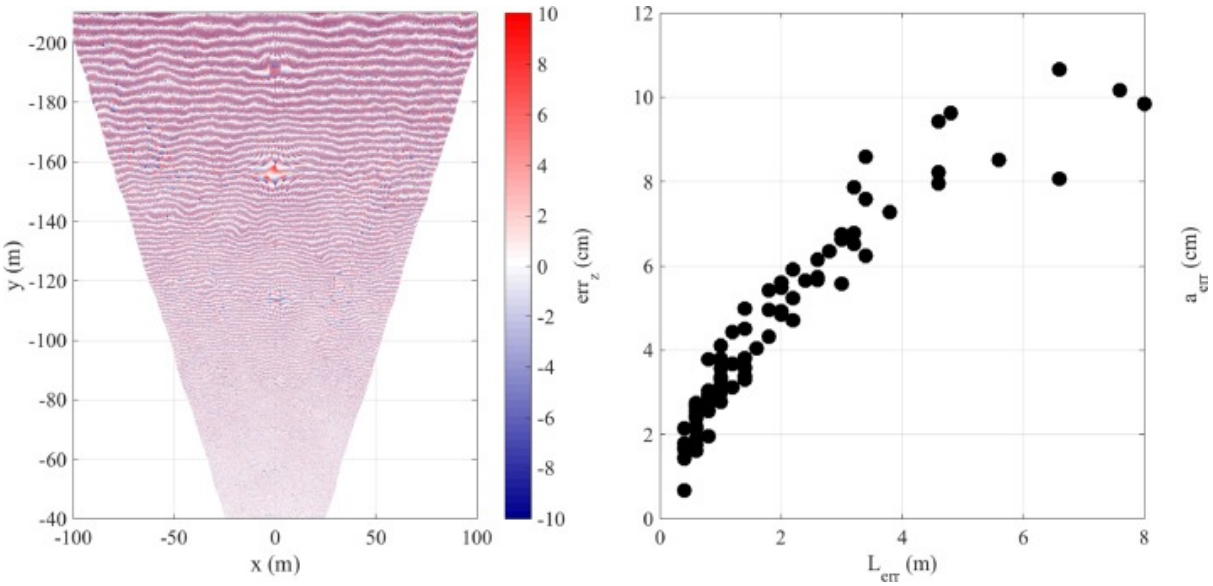

Fig. 25. (left panel) Map of the quantization error (err_z) for sea surface elevations (z-axis) within the horizontal field of view of the stereo cameras. (right panel) Distribution of amplitude a_{err} and wavelength L_{err} of the vertical quantization error along the transect $x = 0$.

To verify the impact on stereo data of the range-dependent quantization error, we have computed the variance density spectrum $S(f_a)$ using a set of time series $z(t)$ taken at increasing range from 40 to 255 m along the y-axis (Fig. 26). We note that there is a very small variability of the energy around the spectral peak and in the high-frequency tail, up to a frequency that depends however upon the range. At 40 m, the departure from a reference slope starts becoming relevant above $f_a = 1.0$ Hz, while at 210 m this frequency is smaller, about 0.7 Hz, that we chose as upper limit to low-pass filter stereo data for the statistical description of the wave field (Section 3.2) and rogue wave analysis (Section 4). As a result, the amplitude of the quantization error shown in Fig. 25 is alleviated on the whole region Γ. Moreover, we observe that also for $f_a < 0.1$ Hz the energetic levels vary with the range; we ascribe this fact to the inhomogeneous reflections that are visible in the far field of the stereo images. However, at the selected range of 210 m, the effect of the low-frequency noise is small, about 0.05 m^2/s, approximately 1/200 of the peak value.

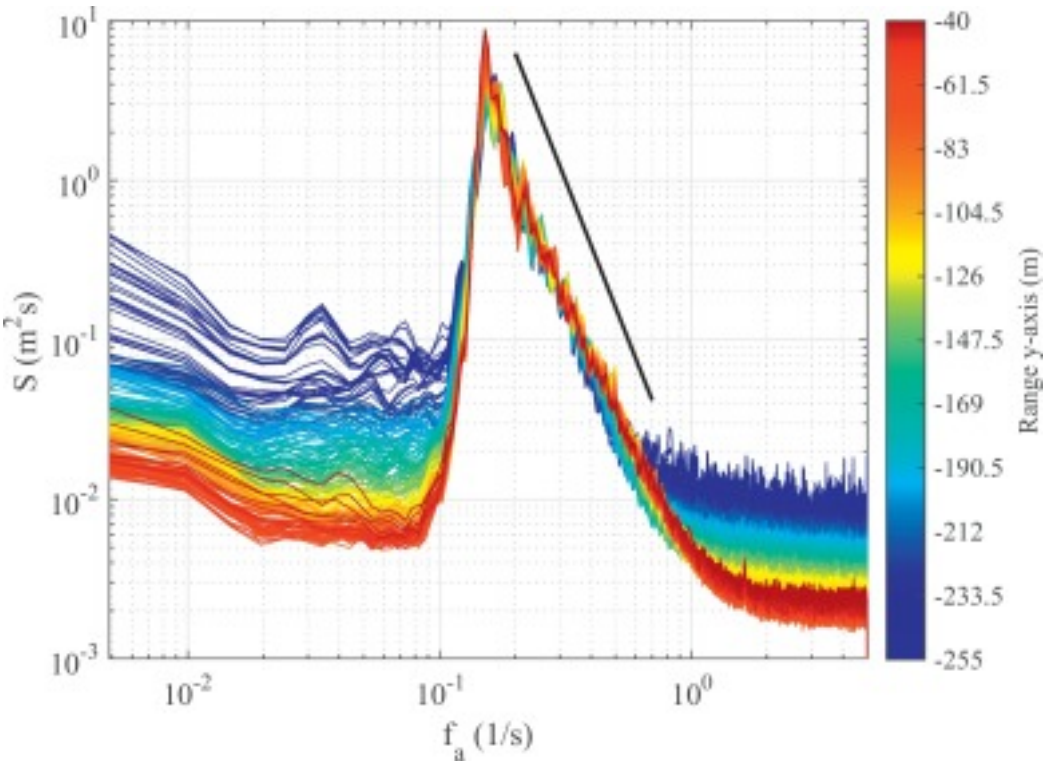

Fig. 26. Omni-directional absolute frequency variance density spectrum $S(f_a)$ color coded for the range along the y-axis of the stereo cameras. The black solid line is the reference spectral slope proportional to f_a^{-4}. (For interpretation of the references to color in this figure legend, the reader is referred to the web version of this article.)

Finally, it is important to evaluate the directional resolution $\Delta\theta$ of the 2-D wavenumber spectrum $S(k_x, k_y)$, which practically limits the capability of properly distinguishing the harmonics with wavelengths comparable to the sides of the analysis window used for the 3-D spectral analysis. Following the approach proposed by Hwang et al., 2000a, Hwang et al., 2000b) the directional resolution is calculated by(29)Δθ=dkxdkykdkwhere dk=dkx2+dky2. For the data presented in this paper, the distribution of Δθ is displayed in Fig. 27, which shows that at $k = k_p = 0.09$ rad/m the resolution is about 25° and becomes better than 10° for $k > 0.25$ rad/m.

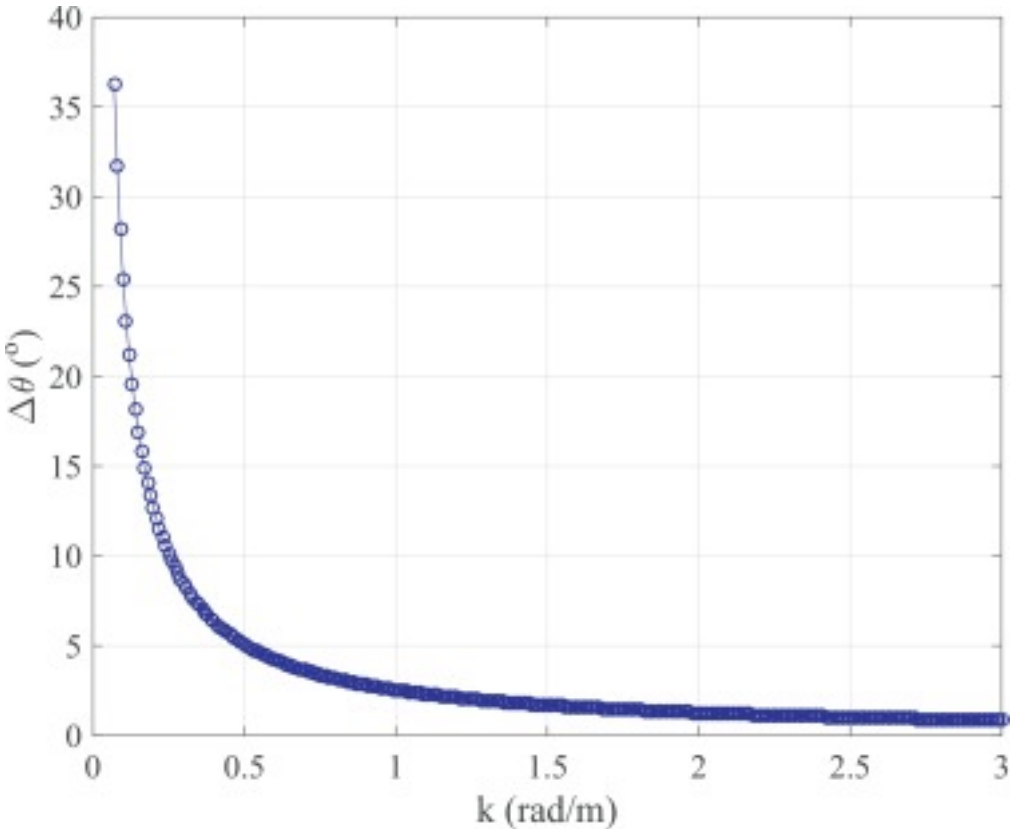

Fig. 27. Directional resolution ($\Delta\theta$) of the 2-D (k_x, k_y)-wavenumber spectrum: dependence on the wavenumber k.

References

R.J. Adler **On excursion sets, tube formulas and maxima of random fields** Ann. Appl. Probab., 10 (2000), pp. 1-74, 10.1214/aoap/1019737664

R.J. Adler, J.E. Taylor **Random Fields and Geometry** Springer, New York (USA) (2007), p. 448

Aubourg, Q., Campagne, A., Peureux, C., Ardhuin, F., Sommeria, J., Viboud, S., Mordant, N., 2017. 3-wave and 4-wave interactions in gravity wave turbulence. arXiv arXiv:1710, 18.

M.L. Banner, I.S.F. Jones, J.C. Trinder **Wavenumber spectra of short gravity waves** J. Fluid Mech., 198 (1989), pp. 321-344

A. Baxevani, I. Rychlik **Maxima for Gaussian seas** Ocean Eng., 33 (2004), pp. 895-911, 10.1016/j.oceaneng.2005.06.006

A. Benetazzo **Measurements of short water waves using stereo matched image sequences** Coast. Eng., 53 (2006), pp. 1013-1032, 10.1016/j.coastaleng.2006.06.012

A. Benetazzo, F. Ardhuin, F. Bergamasco, L. Cavaleri, P. Veras, M. Schwendeman, M. Sclavo, J. Thomson, A. Torsello**On the shape and likelihood of oceanic rogue waves** Sci. Rep., 7 (8276) (2017), pp. 1-11, 10.1038/s41598-017-07704-9

A. Benetazzo, F. Barbariol, F. Bergamasco, C. Sandro, M. Sclavo**Space-time extreme wind waves: analysis and prediction of shape and height** Ocean Modell., 113 (2017), pp. 201-216, 10.1016/j.ocemod.2017.03.010

A. Benetazzo, F. Barbariol, F. Bergamasco, A. Torsello, S. Carniel, M. Sclavo**Stereo wave imaging from a moving vessel: practical use and applications** Coast. Eng., 109 (2016), pp. 114-spo127, 10.1016/j.coastaleng.2015.12.008

A. Benetazzo, F. Barbariol, F. Bergamasco, A. Torsello, S. Carniel, M. Sclavo**Observation of extreme sea waves in a space-time ensemble** J. Phys. Oceanogr., 45 (2015), pp. 2261-2275, 10.1175/JPO-d-15-0017.1

A. Benetazzo, F. Fedele, G. Gallego, P.-C. Shih, A. Yezzi**Offshore stereo measurements of gravity waves** Coast. Eng., 64 (2012), pp. 127-138, 10.1016/j.coastaleng.2012.01.007

F. Bergamasco, A. Torsello, M. Sclavo, F. Barbariol, A. Benetazzo**Computers & geosciences WASS : an open-source pipeline for 3D stereo reconstruction of ocean waves** Comput. Geosci. (2017), pp. 28-36, 10.1016/j.cageo.2017.07.001

P. Boccotti**Wave Mechanics for Ocean Engineering** Elsevier Science B.V. (2000), p. 496

G. Bradski, A. Kaehler**Learning OpenCV: Computer Vision with the OpenCV Library** (2008)

A.J. Campbell, A.J. Beckle, C.H. Wu**Observations of surface waves interacting with ice using stereo imaging**J. Geophys. Res. Ocean, 119 (2014), pp. 3266-3284, 10.1002/2014JC010261.Received

L. Cavaleri, L. Bertotti**Accuracy of the modelled wind and wave fields in enclosed seas** Tellus A, 56 (2004), pp. 167-175

M. Christou, K. Ewans**Field measurements of rogue water waves** J. Phys. Oceanogr., 44 (2014), pp. 2317-2335, 10.1175/JPO-D-13-0199.1

C. Cox, W. Munk**Measurement of the roughness of the sea surface from photographs of the sun's glitter** J. Opt. Soc. Am., 4 (1954), pp. 838-850

S. de Vries, D.F. Hill, M.a. de Schipper, M.J.F. Stive**Remote sensing of surf zone waves using stereo imaging** Coast. Eng., 58 (2011), pp. 239-250, 10.1016/j.coastaleng.2010.10.004

M.A. Donelan, A.-K. Magnusson**The making of the Andrea wave and other rogues** Sci. Rep., 7 (2017), p. 44124, 10.1038/srep44124

L. Draper**"Freak" ocean waves**Oceanus, 10 (1964), pp. 13-15

K. Dysthe, H.E. Krogstad, P. Müller **Oceanic rogue waves** Annu. Rev. Fluid Mech., 40 (2008), pp. 287-310, 10.1146/annurev.fluid.40.111406.102203

F. Fedele**Space–time extremes in short-crested storm seas** J. Phys. Oceanogr., 42 (2012), pp. 1601-1615, 10.1175/JPO-d-11-0179.1

F. Fedele, A. Benetazzo, G. Gallego, P.-C. Shih, A. Yezzi, F. Barbariol, F. Ardhuin**Space–time measurements of oceanic sea states** Ocean Model., 70 (2013), pp. 103-115, 10.1016/j.ocemod.2013.01.001

F. Fedele, J. Brennan, Sonia Ponce de León, J. Dudley, F. Dias**Real world ocean rogue waves explained without the modulational instability** Sci. Rep., 6 (2016), pp. 1-11

F. Fedele, G. Gallego, A. Yezzi, A. Benetazzo, L. Cavaleri, M. Sclavo, M. Bastianini**Euler characteristics of oceanic sea states** Math. Comput. Simul., 82 (2012), 10.1016/j.matcom.2011.05.009

F. Fedele, C. Lugni, A. Chawla**The sinking of the El Faro : predicting real world rogue waves during Hurricane Joaquin** Sci. Rep., 7:11188 (2017), pp. 1-15, 10.1038/s41598-017-11505-5

F. Fedele, M.A. Tayfun**On nonlinear wave groups and crest statistics** J. Fluid Mech., 620 (2009), pp. 221-239, 10.1017/S0022112008004424

G.Z. Forristall**Wave crest distributions: observations and second-order theory** J. Phys. Oceanogr., 30 (2000), pp. 1931-1943

G. Gallego, A. Benetazzo, A. Yezzi, F. Fedele**Wave statistics and spectra via a variational wave acquisition stereo system** ASME 2008 27th International Conference on Offshore Mechanics and Arctic Engineering (2008), pp. 801-808

G. Gallego, A. Yezzi, F. Fedele, A. Benetazzo**A variational stereo method for the three-dimensional reconstruction of ocean waves**

Gemmrich, J. Thomson **Observations of the shape and group dynamics of rogue waves** Geophys. Res. Lett., 44 (2017), pp. 1-8, 10.1002/2016GL072398

S. Hasselmann, C. Bruning, K. Hasselmann, P. Heimbach**An improved algorithm for the retrieval of ocean wave spectra from synthetic aperture radar image spectra** J. Geophys. Res., 101 (1996), pp. 16615-16629

S. Haver**A possible freak wave event measured at the Draupner jacket January 1 1995** Proc. Rogue Waves. 20-22 October, Brest, France (2004)

H. Hirschmüller**Stereo processing by semiglobal matching and mutual information** IEEE Trans. Pattern Anal. Mach. Intell., 30 (2008), pp. 328-341

L.H. Holthuijsen **Waves in Oceanic and Coastal Waters** Cambridge University Press (2007), p. 387

L.H. Holthuijsen**Stereophotography of ocean waves** Appl. Ocean Res., 5 (1983), pp. 204-209, 10.1016/0141-1187(83)90034-2

P.A. Hwang**Doppler frequency shift in ocean wave measurements: frequency downshift of a fixed spectral wave number component by advection of wave orbital velocity** J. Geophys. Res. Ocean., 111 (2006), pp. 1-4, 10.1029/2005JC003072

P.A. Hwang, D.W. Wang, E.J. Walsh, W.B. Krabill, R.N. Swift**Airborne measurements of the wavenumber spectra of ocean surface waves. Part I : spectral slope and dimensionless spectral coefficient** J. Phys. Oceanogr. (2000), pp. 2753-2767

P.A. Hwang, D.W. Wang, E.J. Walsh, W.B. Krabill, R.N. Swift**Airborne measurements of the wavenumber spectra of ocean surface waves. Part II : directional distribution** J. Phys. Oceanogr., 30 (2000), pp. 2768-2787

B. Jähne**Spatio-Temporal Image Processing: Theory and Scientific Applications** (Lecture Notes in 863 Computer Science) (1993)

B. Jähne, J. Klinke, S. Waas**Imaging of short ocean wind waves: a critical theoretical review** J. Opt. Soc. Am. A Opt. Image Sci. Vis., 11 (1994), pp. 2197 2209, 10.1364/JOSAA.11.002197

P.A.E.M. Janssen **On some consequences of the canonical transformation in the Hamiltonian theory of water waves** J. Fluid Mech., 637 (2009), pp. 1-44, 10.1017/S0022112009008131

P.A.E.M. Janssen **Progress in ocean wave forecasting** J. Comput. Phys., 227 (2008), pp. 3572-3594

G.M. Jenkins, D.G. Watts**Spectral Analysis and Its Applications** Holden-Day, San Francisco (1968)

J.T. Kirby, T.M. Chen**Surface-waves on vertically sheared flows: approximate dispersion relations** J. Geophys. Res. Ocean, 94 (1989), pp. 1013-1027

G.J. Komen, L. Cavaleri, K.H. M. Donelan, S. Hasselmann, P.A.E.M. Janssen**Dynamics and Modelling of Ocean Waves** Cambridge University Press (1994)

KORDI Korean Ocean Research and Development Institute**Observation and Investigation of Sea Surface Waves Around Korea** (2003), p. 134 National R&D Report (in Korean)

M.V Kosnik, V.a Dulov**Extraction of short wind wave spectra from stereo images of the sea surface** Meas. Sci. Technol., 22 (015504) (2011), pp. 1-9, 10.1088/0957-0233/22/1/015504

H.E. Krogstad, J. Liu, H. Socquet-Juglard, K. Dysthe, K. Trulsen**Spatial extreme value analysis of nonlinear simulations of random surface waves** Proceedings of OMAE04 23rd International Conference on Offshore Mechanics and Arctic Engineering (2004), pp. OMAE2004-OMA51336

F. Leckler, F. Ardhuin, C. Peureux, A. Benetazzo, F. Bergamasco, V. Dulov**Analysis and interpretation of frequency-wavenumber spectra of young wind waves** J. Phys. Oceanogr., 45 (2015), pp. 2484-2496, 10.1175/JPO-d-14-0237.1

G. Lindgren **Local maxima of Gaussian fields** Ark. Mat., 10 (1972), pp. 195-218

G. Lindgren **Some properties of a normal process near a local maximum** Ann. Math. Stat., 41 (1970), pp. 1870-1883

G. Lindgren, I. Rychlik, M. Prevosto**Stochastic Doppler shift and encountered wave period distributions in Gaussian waves** Ocean Eng., 26 (1999), pp. 507-518

M.S. Longuet-Higgins **On the joint distribution of the periods and amplitudes of sea waves** J. Geophys. Res., 80 (1975), pp. 2688-2694

M.S. Longuet-Higgins**The effect of nonlinearities on statistical distribution in the theory of sea waves** J. Fluid Mech., 17 (1963), pp. 459-480

M.S. Longuet-Higgins**The statistical analysis of a random, moving surface** Proc. R. Soc. London, 249 (1957), pp. 321-387

M.S. Longuet-Higgins, R.H. Stewart**Changes in the form of short gravity waves on long waves and tidal currents** J. Fluid Mech., 8 (1960), pp. 565-583

A.K. Magnusson, M.a. Donelan**The Andrea wave characteristics of a measured north sea rogue wave** J. Offshore Mech. Arct. Eng., 135 (2013), pp. 1-10, 10.1115/1.4023800

A.S. Mironov, M.V. Yurovskaya, V.A. Dulov, D. Hauser, C.A. Guérin**Statistical characterization of short wind waves from stereo images of the sea surface** J. Geophys. Res., 117 (2012), p. C00J35, 10.1029/2011JC007860

J.C. Nieto Borge, G.R. Rodriguez, K. Hessner, P.I. Gonzalez**Inversion of marine radar images for surface wave analysis** J. Atmos. Ocean. Technol., 21 (2004), pp. 1291-1300

H. Nobach, M. Honkanen**Two-dimensional Gaussian regression for sub-pixel displacement estimation in particle image velocimetry or particle position estimation in particle tracking velocimetry** Exp. Fluids, 38 (2005), pp. 511-515, 10.1007/s00348-005-0942-3

S.-H. Oh, W.-M. Jeong, S.-I. Kim**Analysis of the observation data for winter-season high waves occurred in the west sea of Korea** J. Korean Soc. Coast. Ocean Eng., 27 (2015), pp. 168-174

C. Peureux, A. Benetazzo, F. Ardhuin**Note on the directional properties of meter-scale gravity waves** Ocean Sci., 14 (2018), pp. 41-52, 10.5194/os-2017-48

O.M. Phillips**Spectral and statistical properties of the equilibrium range in wind-generated gravity waves** J. Fluid Mech., 156 (1985), pp. 505-531

W.J. Pierson, G. Neumann, R.W. James**Practical Methods for Observing and Forecasting Ocean Waves by Means of Wave Spectra and Statistics**
U.S. Navy Hydrogr. Off. Publ., Washington (1955), p. 284

V.I. Piterbarg**Asymptotic Methods in the Theory of Gaussian Processes and Fields**
Translations of Mathematical Monographs (1996), p. 206

W.J. Plant**The ocean wave height variance spectrum: wavenumber peak versus frequency peak** J. Phys., 39 (2009), pp. 2382-2383, 10.1175/2009JPO4268.1

S.O. Rice**Mathematical analysis of random noise**Selected Papers on Noise and Stochastic Processes (1954), pp. 133-294

J.J. Rodriguez, J.K. Aggarwal**Stochastic analysis of stereo quantization error**
IEEE Trans. Pattern Anal. Mach. Intell., 12 (1990), pp. 467-470

L. Romero, W.K. Melville**Spatial statistics of the sea surface in fetch-limited conditions**
J. Phys. Oceanogr., 41 (2011), pp. 1821-1841, 10.1175/2011JPO4535.1

L. Romero, W.K. Melville**Airborne observations of fetch-limited waves in the Gulf of Tehuantepec** J. Phys. Oceanogr., 40 (2010), pp. 441-465, 10.1175/2009JPO4127.1

M. Schwendeman, J. Thomson**Sharp-crested breaking surface waves observed from a ship-based stereo video system** J. Phys. Oceanogr., 47 (2017), pp. 775-792

C.M. Senet, J. Seemann, F. Ziemer**The near-surface current velocity determined from image sequences of the sea surface** IEEE Trans. Geosci. Remote Sens., 39 (2001), pp. 492-505

F. Serafino, C. Lugni, F. Soldovieri**A novel strategy for the surface current determination from marine X-band radar data** IEEE Geosci. Remote Sens. Lett., 7 (2010), pp. 231-235

R.H. Stewart, W.J. Joy**HF radio measurements of surface currents** Deep. Res., 21 (1974), pp. 1039-1049

M.A. Tayfun**High-wave-number/frequency attenuation of wind-wave spectra** J. Waterw., 116 (1990), pp. 381-398 Port, Coastal, Ocean Eng. 1990 Vol. 116, Issue 3 (381 - 398)

M.A. Tayfun**Narrow-band nonlinear sea waves** J. Geophys. Res., 85 (1980), pp. 1548-1552, 10.1029/JC085iC03p01548

M.A. Tayfun, F. Fedele**Wave-height distributions and nonlinear effects**
Ocean Eng., 34 (2007), pp. 1631-1649, 10.1016/j.oceaneng.2006.11.006

T. Yanagi, K. Inoue**Tide and tidal current in the Yellow/East China Seas** La mer, 32 (1994), pp. 153-165

I.R. Young, S. Hasselmann, K. Hasselmann**Computations of the response of a wave spectrum to a sudden change in wind direction** J. Phys. Oceanogr., 17 (1987), pp. 1317-1338

I.R. Young, W. Rosenthal, F. Ziemer**A three-dimensional analysis of marine radar images for the determination of ocean wave directionality and surface currents** J. Geophys. Res., 90 (1985), pp. 1049-1059

V.E. Zakharov, N.N. Filonenko**Energy spectrum for stochastic oscillations of the surface of a liquid** Sov. Phys. Dokl., 11 (1967), pp. 881-883

A. Zavadsky, A. Benetazzo, L. Shemer**On the two-dimensional structure of short gravity waves in a wind wave tank** Phys. Fluids, 29 (2017), Article 016601, 10.1063/1.4973319